Particle Physics at CERN
Annual Report 2002

C. Amsler, A. Dorokhov, A. Glauser, C. Hörmann, O. Iannarelli, D. Lindelöf,
O. Link, N. Madsen, K. Prokofiev, H. Pruys, C. Regenfus, P. Robmann,
T. Speer and S. Steiner

Physik-Institut der Universität Zürich,
Winterthurerstrasse 190, CH-8057 Zürich, Switzerland

April 4, 2003

Contents

1 Production and Spectroscopy of Antihydrogen

C. Amsler, A. Glauser, O. Iannarelli, D. Lindelöf, N. Madsen, H. Pruys, and C. Regenfus

In collaboration with: CERN, University of Aarhus, Brescia, Genoa, Pavia,
Rio de Janeiro, Swansea, Tokyo (ATHENA Collaboration).

1.1 Introduction

The final goal of the ATHENA experiment is a test of the CPT symmetry in the baryon and lepton sectors by comparing the energy levels of antihydrogen and hydrogen atoms. The long lifetime (122 ms) of the metastable (anti-) hydrogen 2s level is associated with a relative natural line width of $5{\times}10^{-16}$ for the 1s-2s transition, which can be exploited by two-photon laser spectroscopy. Such high precision measurements would also give valuable experimental information on the gravitational interaction of antihydrogen, because a change in the 1s-2s transition frequency could also originate from a different redshift of antihydrogen and hydrogen atoms in the gravitational field of the earth.

Antihydrogen forms when antiprotons are mixed with cold positrons. In 2001-2002 we demonstrated trapping, cooling and transfer of $\sim 10^4$ cold antiprotons into the mixing trap. In the positron accumulator 150 million positrons were routinely accumulated within 5 minutes. Excellent vacuum conditions could be maintained during and after the transfer process, with a lifetime of antiprotons and positrons exceeding several hours. In 2002 we demonstrated for the first time the production of cold antihydrogen atoms in large quantities [1]. The observation of antihydrogen through its annihilation was achieved with the high granularity detector built in our institute. These results were obtained following improvements to the apparatus, in particular a more efficient positron transfer, the implementation of non-destructive plasma diagnostics, and better signal-to-noise ratio for 511 keV photon detection.

Antihydrogen was produced with $\bar{p}e^+$ mixing cycles of about 3 minutes duration which could be repeated every 500 seconds thanks to our fast positron accumulator. At the beginning of each mixing cycle about 10'000 $\bar{p}$ with kinetic energy of $\sim$ 50 eV entered a large and dense positron plasma of typically 70 million e^+. Rapid cooling of the antiprotons in less than 100 msec was observed and the antihydrogen detector registered a rapid increase in the annihilation rate. From the analysis of several hundred cycles a clear signal was identified from unconfined neutral antihydrogen atoms hitting the trap wall. The antihydrogen signal disappeared when the positron plasma was heated to 3500 K.

We refer to previous annual reports and to the experimental proposal [2] for details on the apparatus.

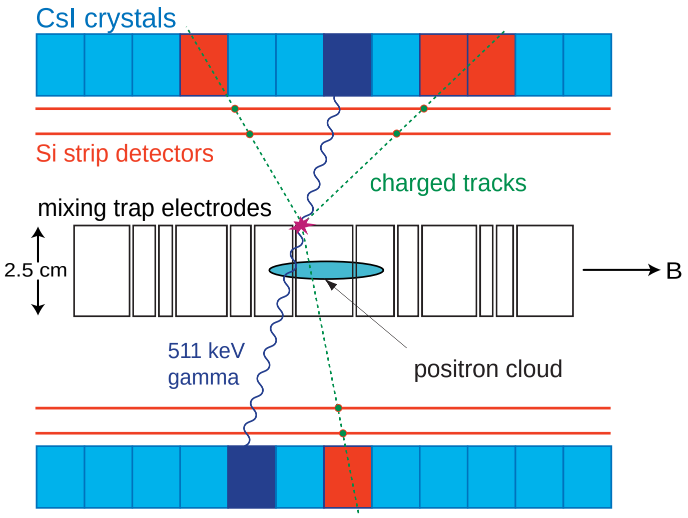

Figure 1.1: *Principle of antihydrogen detection (see text).*

1.2 Development of the antihydrogen detector

The detector (fig. 1.1) features two cylindrical layers of double-sided silicon microstrips (8192 channels) and 16 rows of 12 pure CsI crystals ($17 \times 13 \times 17.5$ mm^3) read out by avalanche photodiodes. It is located in the small space between the (37 mm diameter) UHV vessel of the combination trap and the (70 mm diameter) cold bore of the 3 T superconducting magnet, where vacuum conditions of 10^{-7} mbar and a temperature of 140 K prevail.

The antiproton and positron cease to be confined in the combination trap once bound to antihydrogen. The antiatom therefore collides after less than 1 μs with the surface of the trap electrode. On average three charged pions and three high energy (50-500 MeV) photons are produced by the annihilation of the antiproton, while the positron annihilates with an electron, generating two back-to-back 511 keV photons. The unique identification of antihydrogen is based on the 180° opening angle between the two 511 keV photons, as seen from the antiproton annihilation vertex. A 5μs timing coincidence between the detection of the pions and two 511 keV photons is also required.

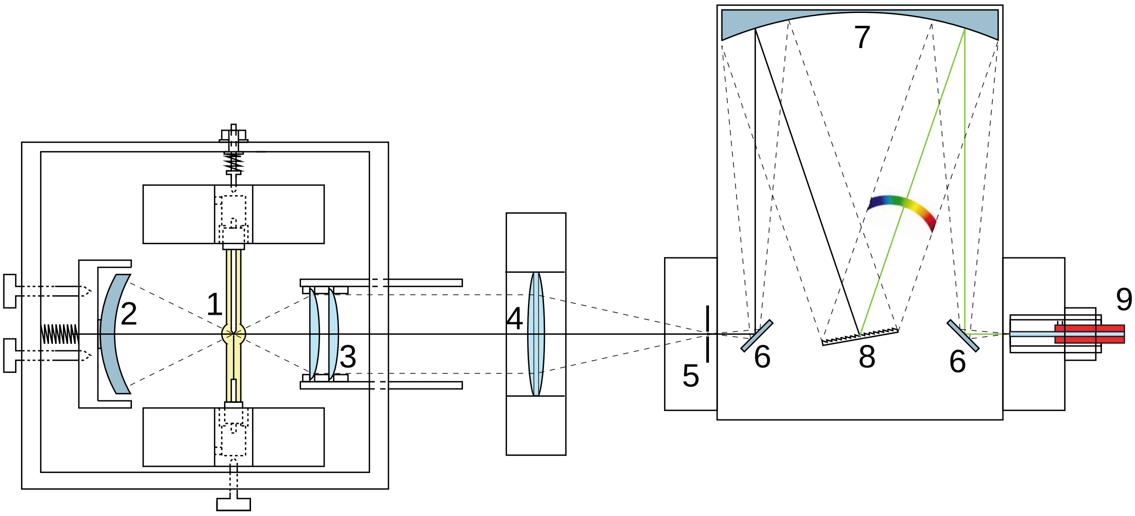

Figure 1.2: *Optical spectrometer. 1: Xenon short arc lamp, 2: spherical mirror, 3: achromator lenses, 4: focussing lens, 5: entrance slit of the monochromator, 6: plane mirrors, 7: spherical mirror, 8: Echelette grating, 9: fiber (after [4]).*

Pure CsI was chosen because of the excellent light yield at low temperature (50’000 photons/MeV at 80 K [3]), together with a total absorption probability of 20% for 511 keV photons. Initially, the crystals were coupled to pn photodiodes, but the quantum efficiency decreased dramatically below 450 nm, especially at low temperatures. A systematic study of this effect was undertaken by building an optical spectrometer based on an Echelette grating (fig. 1.2) [4]. The selected light (resolution of 2 nm FWHM) exiting the spectrometer was transferred by an optical fiber to a liquid nitrogen cell containing the test photodiodes. Figure 1.3 shows the relative quantum efficieny as a function of temperature and wavelength (a unit relative efficiency corresponds to an absolute efficiency of 62%, obtained by comparison with a commercially calibrated photodiode). One observes a fast drop in the detection efficiency of blue light with decreasing temperature. The reason for this behaviour is not quite understood.

In addition, the performance of our photodiodes deteriorated with time (apparently due to corrosion from the iodine in CsI). In 2002 we therefore replaced all photodiodes by avalanche photodiodes (APD) which have the advantage of a large gain and hence a much better signal-over-noise ratio. Figure 1.4 shows a photograph of one of the 300 APD’s purchased from CMS (a small batch from their 160’000 supply!). The gain of the APD as a function of bias voltage was measured with a pulsed light

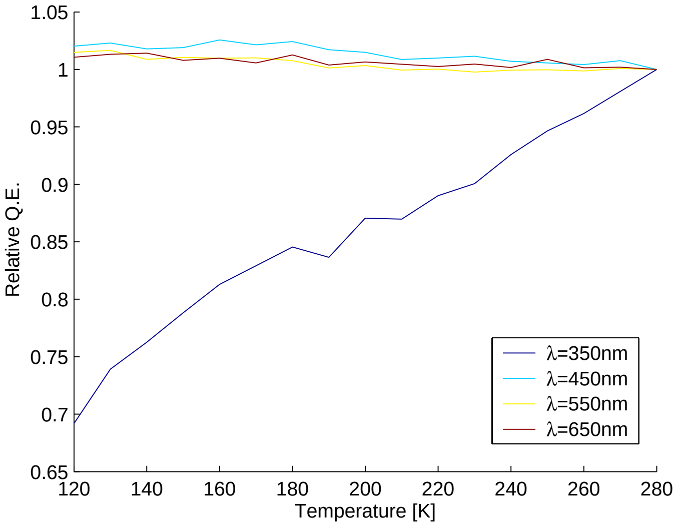

Figure 1.3: *Relative quantum efficiency of a photodiode as a function of temperature and wavelength.*

emitting photodiode (fig. 1.5). The plateau at low voltage corresponds to unit gain, the rise is due to the generated avalanche in the diode. The voltage at which multiplication starts depends on temperature, due to mobility which is a function of temperature. The advantage of APD's for ATHENA is the very low dark current at low temperature, so that the signal can be amplified to very high values. We settled for a gain of 20 corresponding to a signal-over-noise ratio of about 100.

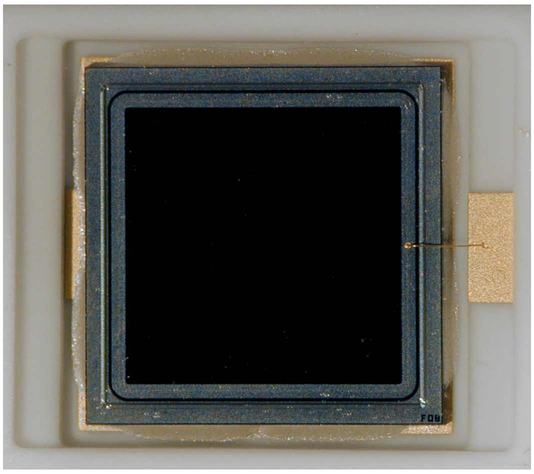

Figure 1.4: *Avalanche photodiode (5 × 5 mm^2) purchased from the CMS experiment. The epoxy window was removed with sulfuric acid.*

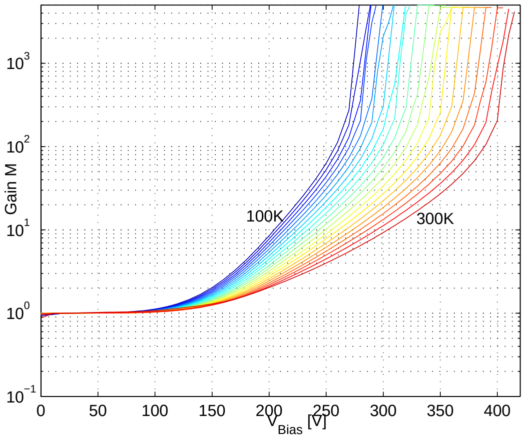

Figure 1.5: *Gain of an avalanche photodiode as a function of bias voltage V for different temperatures. The curves are fits with exponential functions of the form* $a + b\,\exp(cV)$.

The detector is now working to our full satisfaction. Figure 1.6 shows the measured photon energy spectrum with APDs from positron annihilation in the combination trap, summed over all crystals. The peak at 511 keV has a resolution of 18% FWHM and is well separated from the Compton plateau and the noise.

1.3 Positron heating

Characteristics of the positron plasma such as shape, dimension, density and temperature, are important parameters for the antiproton-positron interaction. For instance, the temperature dependence of

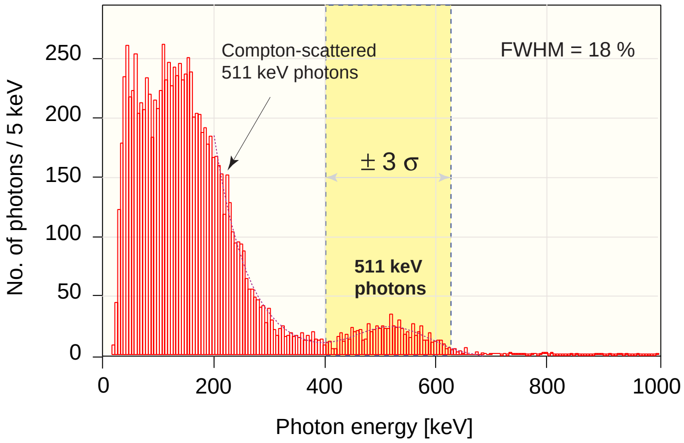

Figure 1.6: *Measured photon energy distribution for positron annihilation in the combination trap (sum over all 192 crystals).*

antihydrogen formation depends crucially on the formation mechanism, spontaneous radiative transitions (which populates the lower energy levels) or three-body combination (which populates the higher energy states).

The positron plasma is confined in the central part of the mixing trap by the harmonic axial potential. The positrons cool to the ambient temperature of the surrounding trap walls ($\simeq$ 15 K) through synchrotron radiation in the 3 T magnetic field, with a typical time constant of 400 msec. The shape of the plasma is a prolate ellipsoid, 3 cm long and 4 mm in diameter, with a density of $2.5\times\ 10^8$ cm^{-3}. We use a non-destructive diagnostic to control and monitor the positron plasma parameters. It is based on the excitation of the first two axial resonant plasma oscillation modes (dipole, quadrupole) by applying a sinusoidal perturbation to one electrode, and then observing the induced current in a pick-up electrode [5]. The plasma density and shape of the plasma is extracted from the measured frequencies of the dipole and quadrupole modes [6]. By applying an RF signal to one of the trap electrodes that sweeps a frequency band near the dipole frequency (21 MHz), the plasma can be heated in a controlled way, depending on the heating amplitude of typically a few mV. Antihydrogen formation can therefore be controlled and even quenched by controlling the positron plasma temperature. The dependence of the plasma temperature shift ΔT on the excitation voltage V_d was measured and is shown in fig. 1.7.

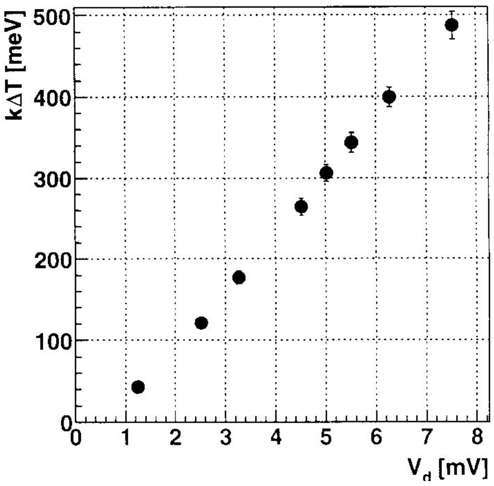

Figure 1.7: *Plasma temperature variation ΔT vs. RF heating amplitude V_d.*

1.4 Antihydrogen production

A positron-antiproton mixing cycle lasts for 500 s and starts with the transfer of about 7×10^7 positrons into the combination trap, where they cool to $\simeq$ 15 K. A W-shaped potential (nested trap) is then formed around the positron plasma. Positrons are confined in the central part of the potential. Simultaneously, 10’000 antiprotons are captured, cooled by electrons in the capture trap and then launched into the combination trap. The antiproton and the positron plasma mix for about 3 minutes, after which all particles are dumped and the process is repeated.

Positron cooling of antiprotons was reported earlier by the ATRAP collaboration [7]. In ATHENA, we studied this process with 10’000 antiprotons crossing a much larger and denser positron plasma. Antiprotons were stored in a side potential well and then launched into the mixing region with a kinetic energy of $\simeq$ 50 eV. Antiprotons traversing the positron plasma loose energy through collisions. Evidence for positron cooling was obtained by lowering the potentials of the side wells in the nested trap and measuring the number of annihilating antiprotons as a function of voltage. The results show that, after a short initial cooling time of $\simeq$ 500 ms, the two plasmas separate both in longitudinal and radial direction, leading to a decreasing overlap and hence interaction between the two antiparticle species.

Annihilation events trigger the silicon detector. In the offline analysis antiproton annihilation vertices are reconstructed from the silicon detector data. For each reconstructed vertex, we search for two well separated 511 keV photon hits in the crystal data. To search for antihydrogen events we calculate the opening angle $\Theta_{\gamma\gamma}$, between the γ-directions. For an antihydrogen event, this angle should be 180°. Figure 1.8 shows an event compatible with antihydrogen annihilation.

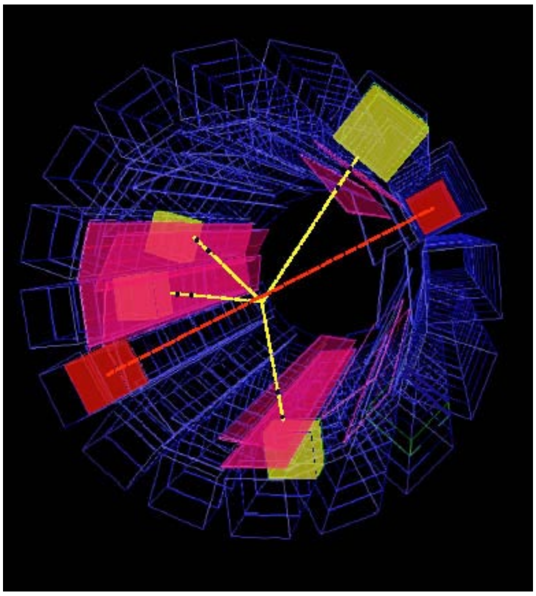

Figure 1.8: *Reconstructed antihydrogen annihilation event with four charged particles from a common vertex, and two isolated 511 keV photons that appear back-to-back when looking from the vertex.*

The spatial resolution on the annihilation vertex is mainly determined by the unknown track curvature in the 3 T magnetic field. The charged particle vertex resolution in radial direction was measured experimentally by letting antiprotons annihilate on the trap electrodes (radius 12.5 mm). The measured distribution agrees well with the Monte Carlo prediction and the radial resolution is $\sigma \simeq 4$ mm. The simulation gives a probability of 50 % for vertex reconstruction, in agreement with measurement. This probability is determined by the solid angle of the outer silicon layer and the trigger and detector efficiencies. The interaction probability of 511 keV photons in a crystal is about 20 %. Taking into account the solid angle of the CsI calorimeter, crystal inefficiencies and all cuts, the detection efficiency for both photons is about 1 %, leading to a total efficiency for event reconstruction of about 0.5 %.

Figure 1.9 shows the opening angle distribution from 165 mixing cycles of antiprotons with cold positrons. The peak at cos $\Theta_{\gamma\gamma}$ = -1 is clearly observed. It contains 131 ± 22 events, corresponding to a statistical significance of more than 5σ. The triangles in fig. 1.9 (left) represent hot mixing data in which no antihydrogen formation is expected. The flat background from spatially uncorrelated two-photon events is due to high-energy photons from antiproton annihilations on the wall, producing electromagnetic showers with secondary positrons. This process does not produce a peak at 180 °.

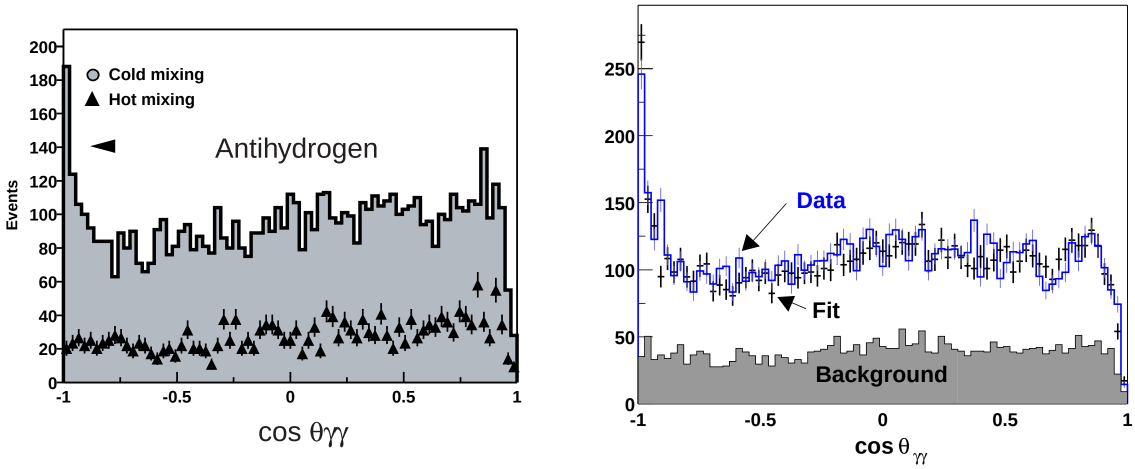

Figure 1.9: *Left: Number of events vs. cosine of the opening angle $\Theta_{\gamma\gamma}$. The histogram is for cold mixing data (7'125 events). The triangles represent hot mixing data, scaled by 1.6 for the same number of mixing cycles (from ref. [1]). Right: Fit of opening angle distribution for cold mixing using simulated data for antihydrogen annihilation and antiproton background from hot mixing (for a slightly larger data sample).*

We have studied the relative contribution of antihydrogen and antiproton annihilations. Antihydrogen atoms annihilate on a trap electrode. On the other hand, antiprotons are confined by the fields and oscillate in the centre of the trap, where they may annihilate with rest gas or with positive ions trapped with the positron plasma. We have measured the $(x - y)$ vertex distribution (fig. 1.10) for antiproton mixing with cold and hot positron plasma. For cold mixing, a clear image of the trap electrodes is obtained, consistent with antihydrogen annihilations on the wall. The distribution for hot mixing, also shown in fig. 1.10, has a very different shape. Antihydrogen production is suppressed, and stored antiprotons annihilate with trapped ions (or with rest gas) in the centre of the trap. The relative contribution of antihydrogen versus antiproton background in the cold mixing data was determined by fitting the $x - y$ distribution with a simple model consisting of two contributions, (i) antihydrogen annihilation on the trap wall (from Monte Carlo simulation) and (ii) antiproton-ion annihilation inside the trap volume (from the hot mixing measurement). The fit gave a relative contribution of 35 ± 10% background in fig. 1.9. The same result is obtained by fitting the $\Theta_{\gamma\gamma}$ distributions for hot and cold mixing. The result is shown in fig. 1.9 (right). Hence about 65 % of the events in the $\Theta_{\gamma\gamma}$ distribution are actually due to antihydrogen formation, where at least one of the two 511 keV γ's stems from background. The data collected in 2002 correspond to the production of about 10^6 antihydrogen atoms in the ATHENA apparatus.

Figure 1.11 shows the number of reconstructed vertices as a function of time during a typical mixing cycle. Immediately after antiproton injection a sharp increase in the number of annihilations is observed by the detector. The event rate is above 100 Hz during the first second. The annihilation rate then decreases slowly to 1 Hz after 3 minutes. Fast cooling antiprotons within the positron cloud lead to a high initial antihydrogen rate. As most of their kinetic energy is lost the remaining antiprotons are located in the side wells or are radially separated from the positron plasma, thus reducing the

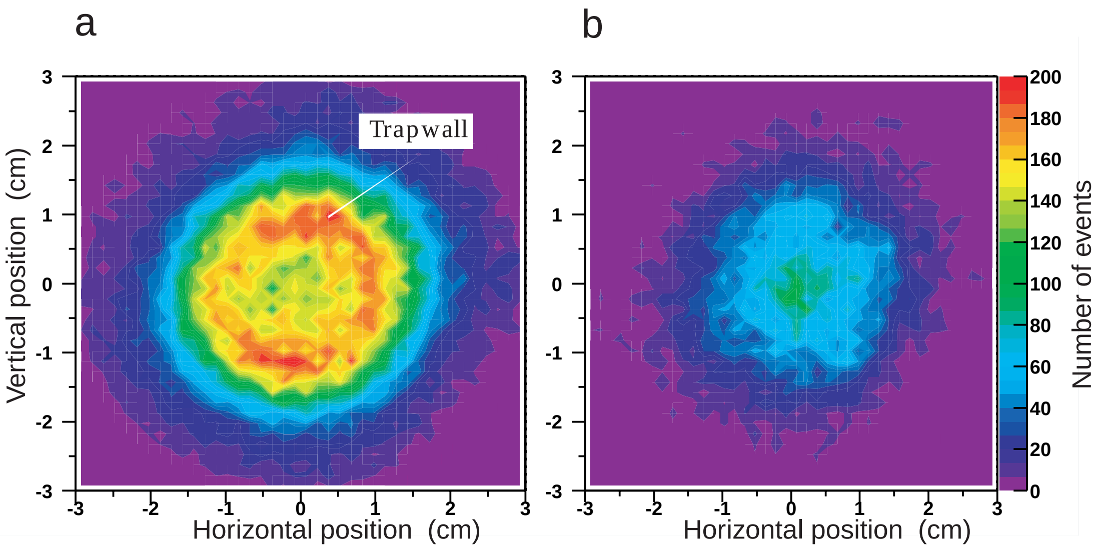

Figure 1.10: *Transverse vertex positions for mixing with cold positrons (left) and hot positrons (right) (from ref. [1]).*

probability of antihydrogen formation.

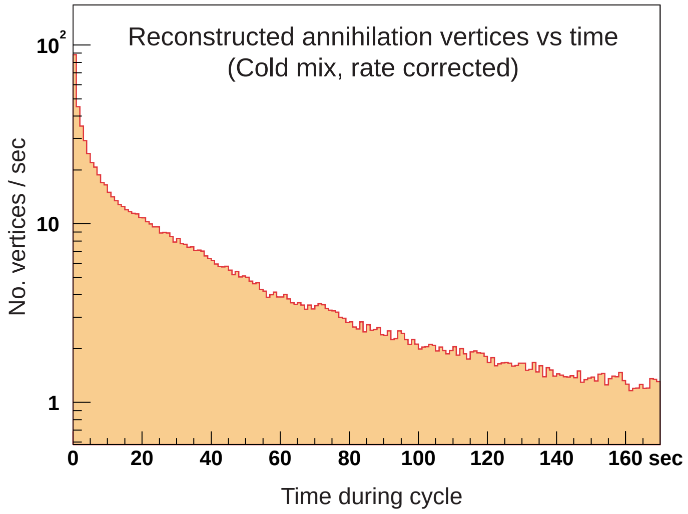

Figure 1.11: *Number of reconstructed annihilation vertices as a function of time after injection of the antiprotons into the positron plasma.*

We studied also the temperature dependence of antihydrogen production. The distributions show that for increasing plasma temperature, the relative size of the back-to-back peak decreases and there is clear evidence that antihydrogen production takes place even at room temperature (30 meV). This speaks in favour of radiative combination as the dominant formation mechanism, since three-body combination is only expected to occur at very low temperatures (much below 10 meV). Furthermore the temperature dependence of antihydrogen production seems to follow the simple $1/T$ dependence consistent with radiative combination. These are very good news for atomic level spectroscopy, since we will require antihydrogen to be in the 1s state.

The dependence on temperature can be used for pulsed antihydrogen production. By switching on the RF heating of positrons, antihydrogen production can be switched off within $\sim$ 100 ms. The positron plasma then cools down by synchrotron radiation after switching the RF heating off, and antihydrogen production resumes within less than 1 second (fig. 1.12).

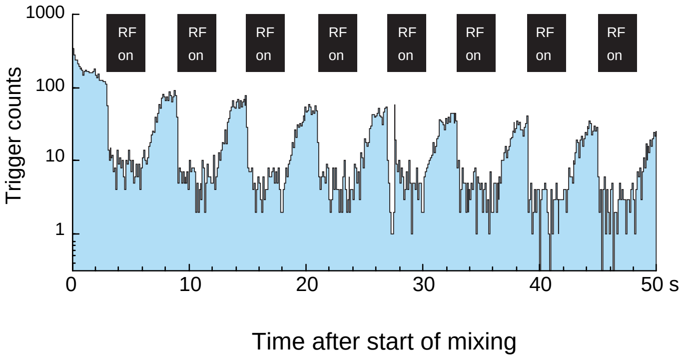

Figure 1.12: *Annihilation trigger rate with and without RF heating of the plasma during 3s intervals.*

1.5 R & D for laser spectroscopy

Until the one year accelerator shutdown in 2005 we will study antihydrogen production and its dependence on parameters such as the number, density and temperature of antiprotons and positrons. Currently roughly 15-20 % of all antiprotons in the mixing trap form antihydrogen, and we are studying ways to increase this number. Stimulated combination by irradiation with laser light is also being investigated.

In 2002 the Zurich group initiated the first part of the spectroscopy phase, the construction of a laser system to generate the 243 nm light for 1s-2s two-photon spectroscopy in antihydrogen [8]. No laser-sources are available in the ultra-violet region. We therefore use a non-linear technique to generate the 243 nm light from a laser source of longer wavelength. Figure 1.13 shows schematically the laser system that is currently being implemented [8]. Most of the equipment was provided by the University of Aarhus. The system consists first of a Coherent Innova Sabre - Kr^+ ion laser that emits 4 W in the range 406 nm to 415 nm. The Kr^+ ion laser pumps a Coherent 899-21 Ring Dye laser that circulates Coumarin 102 dye which emits in the range 460 nm to 516 nm. The dye laser is necessary to introduce tunability in the system, as an ion laser emits only at specific wavelengths. The dye laser is tuned to a wavelength of 486.2 nm which is twice the wavelength of the two-photon 1s-2s transition in antihydrogen. About 500 mW of light is emitted at 486.2 nm.

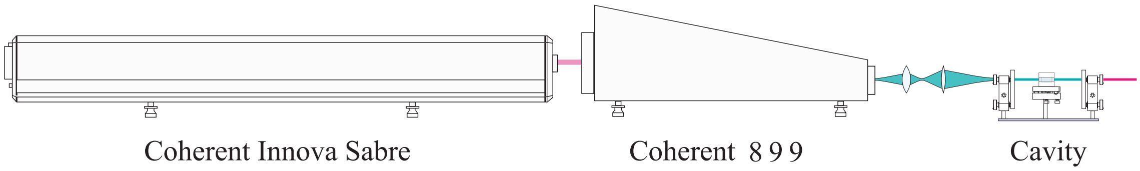

Figure 1.13: *Sketch of the laser chain to generate the 243 nm light for 1s-2s two-photon spectroscopy.*

The light from the dye laser is sent into an external frequency doubling cavity containing a non-linear crystal. The second harmonic generation power in the crystal is maximum when the refractive indices n for the fundamental and the second harmonics are equal. Since the refractive index depends on frequency, a birefringent crystal with a suitably oriented optical axis is used, in which the ordinary ray is chosen for the fundamental frequency and the extraordinary ray for the second harmonic, i.e. $n_o(\omega) = n_e(2\omega)$. Losses are reduced by using a crystal cut such that the light with fundamental frequency traversing the crystal penetrates the crystal under the Brewster angle. Under this angle the polarisation parallel to the plane formed by the incident beam and the normal to the crystal surface is not reflected but transmitted into the crystal.

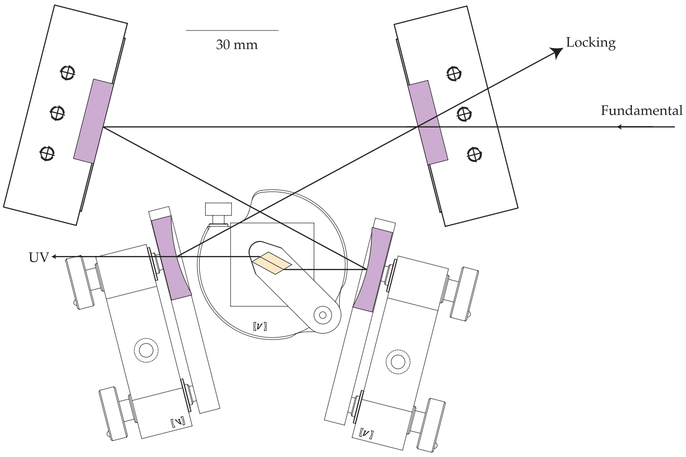

Figure 1.14: *External cavity with BBO crystal (yellow) for second harmonic generation (see text).*

The cavity that was chosen is shown in fig. 1.14 (for details see ref. [8]). It consists of a Brewster cut rhomb shaped beta barium borate (BBO) crystal with a side length of 8 mm. The light from the dye laser enters from the right. The convex mirrors have a reflection coefficient of 100% for the first harmonic and a transmission coefficient of 95 % for the second harmonic. The locking beam is sent to a photodiode for frequency locking. The external cavity is expected to deliver about 50 mW of laser light at 243.1 nm.

In 2002 we installed the clean room and most of the laser system. The various components such as mirrors and the BBO crystal have been purchased. The cavity assembly is close to completion. The setting up of the dye laser was complicated by technical problems. Its operation is now stable but only at about half the nominal power. This is sufficient for the first tests of the frequency doubling, which we expect to commence shortly.

References

[1] M. Amoretti *et al.*, Nature **419** (2002) 456

[2] ATHENA proposal, M.H. Holzscheiter et al., CERN-SPSLC/P302, October 1996, see also http://www.cern.ch/athena/

[3] C. Amsler *et al.*, Nucl. Instr. Meth. in Phys. Res. **A 480** (2002) 494

[4] A. Glauser, Diplomarbeit, Universität Zürich, 2003

[5] M. Amoretti *et al.*, submitted to Phys. Rev. Lett.

[6] D. H. E. Dubin, Phys. Rev. Lett. **66** (1991) 2076

[7] G. Gabrielse *et al.*, Phys. Lett. **B 507** (2001) 1

[8] O. Iannarelli, Diplomarbeit, Universität Zürich, in preparation

2 Measurement of the Neutrino Magnetic Moment at the Bugey Nuclear Reactor

C. Amsler, O. Link and H. Pruys

In collaboration with: Institut des Sciences Nucléaires (Grenoble), Université de Neuchâtel, Università di Padova (MUNU Collaboration).

2.1 Introduction

The MUNU experiment measures the magnetic moment of antineutrinos $\overline{\nu}_e$ from a nuclear reactor, using the elastic scattering reaction $\overline{\nu}_e e^- \rightarrow \overline{\nu}_e e^-$. This process is very sensitive to the magnetic moment of the $\overline{\nu}_e$ (especially at low neutrino and low electron recoil energies) because it is a pure leptonic and theoretically well understood weak process.

In the standard model the magnetic moment vanishes for massless neutrinos. Even for massive ν_e with masses in the range observed recently, the standard model predicts magnetic moments much below 10^{-20} μ_B, which are not accessible experimentally. The experimental evidence for a large magnetic moment would mean new physics beyond the standard model. With a finite magnetic moment the spin of a lefthanded neutrino may flip due to the electromagnetic interaction, and the neutrino become a "sterile" righthanded state which does not interact, and hence is experimentally invisible. The precession of a magnetic moment in the range $\mu_\nu \sim 10^{-10} - 10^{-12}$ μ_B in the solar magnetic field offers an alternative explanation to the MSW effect for the observed deficit of solar neutrinos.

A detailed description of the apparatus can be found in ref. [1, 2] and in previous annual reports. MUNU uses a 1 m^3 time projection chamber (TPC, gaseous CF$_4$ at 3 bar) to measure the scattering angle and the kinetic energy of the recoil electron. The energy threshold for detecting electrons is typically 300 keV. Since the cross section for neutrino reactions is very low, background measurements are important. To reject background events due to cosmic muons and Compton scattering of low energy γ's, the TPC is surrounded by a tank filled with liquid scintillator. The electrons are scattered into the forward hemisphere. To subtract the background, electrons are also measured in the backward hemisphere. Measurements during reactor shutdown were done to check that equal amounts of background electrons are emitted in the forward and backward hemispheres.

2.2 Data analysis

Data taking was completed in 2002. We collected neutrino data during 111 days, corresponding to a livetime of 66.3 days after deadtime subtraction. We also collected reactor off data during 37 days (19.3 days after deadtime subtraction). In addition, calibration data were recorded periodically for various triggers.

A first quick analysis was done by "visual" tracking: every potential neutrino event was examined by eye and the scattering angle and recoil energy were determined. This method, applied by the Neuchâtel group, was restricted to the analysis of recoil electrons with an energy above 700 keV.

A systematic data analysis was performed by the University of Zürich group using a pattern recognition program ("automatic tracking"). With the automatic reconstruction program we were able to analyze larger datasets, e.g. neutrino data with lower electron recoil energies. The software was carefully tested and compared to Monte Carlo simulation [3]. The angular resolution and acceptance were determined from Monte Carlo generated events (see fig. 2.15). The resolution and acceptance become worse at lower energies, mainly due to multiple scattering and electronic noise.

The final analysis is done by comparing the electron rates in the forward hemisphere (neutrino scattering events and background events) with those in the backward hemisphere (background events only).

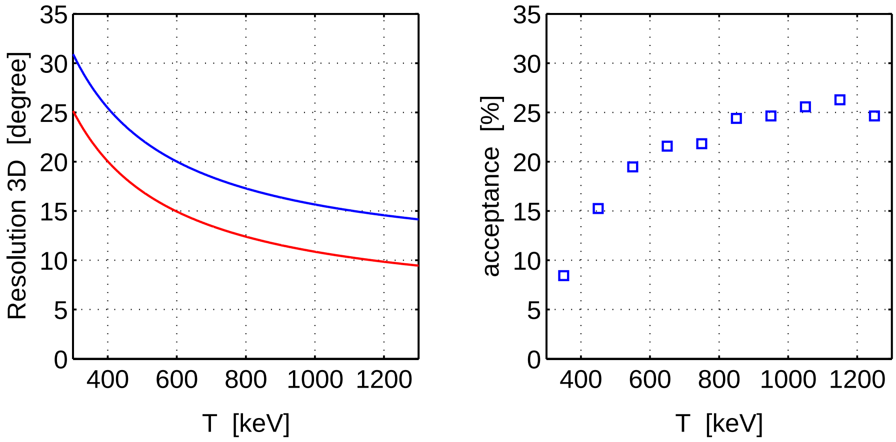

Figure 2.15: *Left: Angular resolution on the direction of the recoil electron as a function of electron energy. Red curve: 3d angular fit with true vertex; blue curve: fit with reconstructed vertex. Right: Acceptance as function of electron energy.*

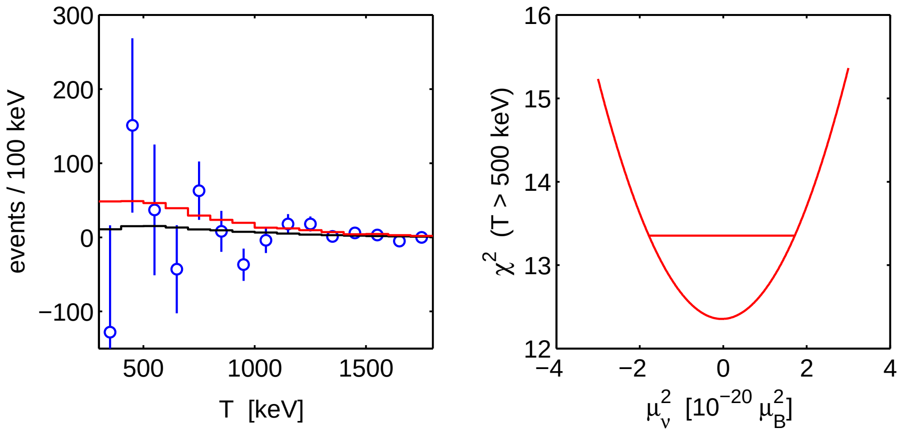

Figure 2.16: *Left: Energy spectrum of forward minus backward events. The data points are compared with Monte Carlo spectra without magnetic moment (black curve) and with a magnetic moment of* $1.7 \times 10^{-10}\mu_B$ *(red curve). Right:* χ^2 *as function of* μ_ν^2 *(fit parameter).*

Figure 2.16 (left) shows the measured forward minus backward intensity as a function of electron energy. The curves show Monte Carlo simulations based on the electroweak theory with no contribution from the neutrino magnetic moment (black) and with a magnetic moment of $1.7 \times 10^{-10}\mu_B$ (red). The Monte Carlo simulation gives the expected number of events per 100 keV as a function of recoil electron energy T

$$MC(T) = W(T) + \mu_\nu^2\, M(T),$$

where the part $W(T)$ is independent of the magnetic moment and the part involving $M(T)$ depends on the square of the magnetic moment. Fitting this expression to the data and using μ_ν^2 as free parameter gives $\mu_\nu^2 = (-0.04 \pm 1.74) \times 10^{-20}\mu_B^2$ (fig. 2.16, right) . Thus there is no indication of a finite magnetic moment. A 90% confidence level upper limit of

$$\mu_\nu < 1.7 \times 10^{-10}\,\mu_B \tag{2.1}$$

is obtained using the unified approach of ref. [4] to obtain an upper limit from gaussian data close to a physical boundary. This upper limit is somewhat smaller than the preliminary limit $2.3 \times 10^{-10}\mu_B$

published by the MUNU collaboration [5] and somewhat larger than the limit $1.4 \times 10^{-10} \mu_B$ obtained by a visual scan above 700 keV. However, our upper limit, eqn. (2.1), is independent of the applied energy threshold (see fig. 2.17). The larger background compensates for the increased sensitivity to μ_ν at lower recoil energies.

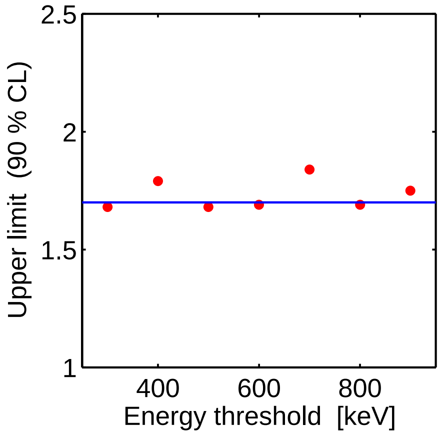

Figure 2.17: *Upper limits on μ_ν (in units of $10^{-10}\mu_B$) as a function of recoil energy threshold.*

Previous laboratory experiments led to upper limits of $\mu_\nu < 1.9 \times 10^{-10}\ \mu_B$ [6] and 1.5×10^{-10} μ_B [7]. The astrophysical upper limits, e.g. from SN1987A, are lower by two orders of magnitude but make assumptions, in particular that the neutrino is a Dirac particle. On the other hand, it is interesting to note that a reanalysis of Reines' Savannah data [8] led to a magnetic moment of the size of our upper limit, when taking into account today's improved knowledge of reactor spectra [9].

The present work is part of a PhD thesis [3]. The apparatus is being dismantled in 2003. This report is therefore the last one on our contribution to the MUNU experiment.

References

[1] C. Amsler *et al.* (MUNU Collaboration), Nucl. Instr. Methods in Phys. Res. **A 396** (1997) 115

[2] M. Avenier *et al.* (MUNU Collaboration), Nucl. Instr. Methods in Phys. Res. **A 482** (2002) 408

[3] O. Link, PhD thesis, Universität Zürich, in preparation

[4] G.J. Feldman and R.R. Cousins, Phys. Rev. **D 57** (1998) 3873

[5] C. Amsler *et al.* (MUNU Collaboration), Phys. Lett. **B 545** (2002) 57

[6] A. I. Derbin *et al.*, JETP Lett. **57** (1993) 768

[7] J .F. Beacom and P. Vogel, Phys. Rev. Lett. **83** (1999) 5222

[8] F. Reines, H. S. Gurr and H. W. Sobel, Phys. Rev. Lett. **37** (1976) 315

[9] P. Vogel and J. Engel, Phys. Rev. **D 39** (1989) 3378

3 The scalar glueball

C. Amsler

The Crystal Barrel experiment which ran at CERN's Low Energy Antiproton Ring until 1996 discovered several new mesons, among them the $J^{PC} = 0^{++}$ isoscalar meson $f_0(1500)$ and the 0^{++} isovector $a_0(1450)$ (for a review see ref. [1]). We have shown several years ago that the $f_0(1500)$ was an excellent candidate for the ground state glueball expected by lattice gauge theories around this mass [2]. In the present report we argue that recent results from LEP indicate that $f_0(1500)$ couples only weakly to photons. This strengthens the evidence that $f_0(1500)$ contains a large fraction of glue. On the other hand, a reasonable $q\overline{q}$ nonet for the scalar mesons can be built with the other known mesons, among them the $f_0(1710)$ which appears to be the $s\overline{s}$ state in the nonet [3].

The $f_0(1370)$ and $f_0(1500)$ mesons were established by Crystal Barrel, first in their $\eta\eta$ and $\pi^0\pi^0$ decay modes [4]. The $f_0(1370)$ is broad (~ 400 MeV) while the $f_0(1500)$ is rather narrow (~ 100 MeV). Their $K\bar{K}$ decay rates were measured by Crystal Barrel [5]. They are small compared to $\pi\pi$, indicating that neither state can have a large $s\overline{s}$ component [3].

The WA102 Collaboration at CERN observed the $f_0(1370)$, $f_0(1500)$ and $f_0(1710)$ decaying to $K\bar{K}$ and $\pi\pi$ in pp central production at 450 GeV [6]. For $f_0(1370)$ and $f_0(1500)$, the $\pi\pi$ decay mode was favoured over $K\overline{K}$. Hence both $f_0(1370)$ and $f_0(1500)$ do not have large $s\bar{s}$ components, in agreement with Crystal Barrel results. However, for $f_0(1710)$, $K\bar{K}$ decay dominates $\pi\pi$ by a large factor, suggesting that this state must be dominantly $s\overline{s}$.

The $f_0(1710)$ was also searched for in $\overline{p}p$ annihilation into three pseudoscalar mesons with 900 MeV/c antiprotons [7]. For example, in $\overline{p}p \to \pi^0\eta\eta$ the $f_0(1710) \to \eta\eta$ is not observed, while $f_0(1500)$ is clearly seen. This is prima facie evidence that $f_0(1710)$ cannot have a large $u\overline{u} + d\overline{d}$ component.

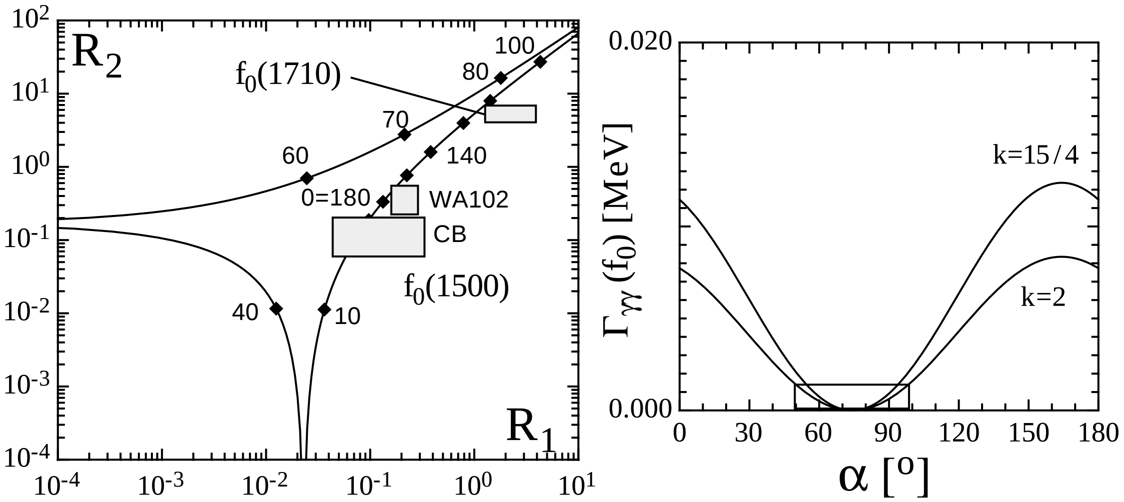

Figure 3.1: Left: relative decay branching ratio $R_2 = B(K\overline{K})/B(\pi\pi)$ vs. $R_1 = B(\eta\eta)/B(\pi\pi)$ as a function of mixing angle α (in deg.); right: predicted $\gamma\gamma$-width for the $f_0(1500)$. The experimental upper limit is shown by the box (from ref.[3]).

For a more quantitative statement, look at fig. 3.1 (left) which shows the ratio of branching ratios $R_2 = B(K\overline{K})/B(\pi\pi)$ vs. $R_1 = B(\eta\eta)/B(\pi\pi)$ for scalar mesons, apart from phase space factors. Data from Crystal Barrel and WA102 (2σ boundaries) on the $f_0(1500)$ and $f_0(1710)$ are compared with predictions from SU(3). The angle α describes the mixing of the two nonet isoscalar mesons,

$$|f_0\rangle = \cos\alpha\,|n\overline{n}\rangle - \sin\alpha\,|s\overline{s}\rangle \quad \text{with} \quad |n\overline{n}\rangle \equiv \frac{u\overline{u} + d\overline{d}}{\sqrt{2}}\ . \tag{3.1}$$

Hence for α = 0, f_0 is pure $n\overline{n}$ and for α = 90°, pure $s\overline{s}$. Assuming that $f_0(1500)$ and $f_0(1710)$ are $q\overline{q}$ states, we conclude from fig. 3.1 (left) that the former is mainly $n\overline{n}$ (-10° $\leq \alpha \leq$ 5°) and the latter mainly $s\overline{s}$ ($\alpha \simeq$ 117°).

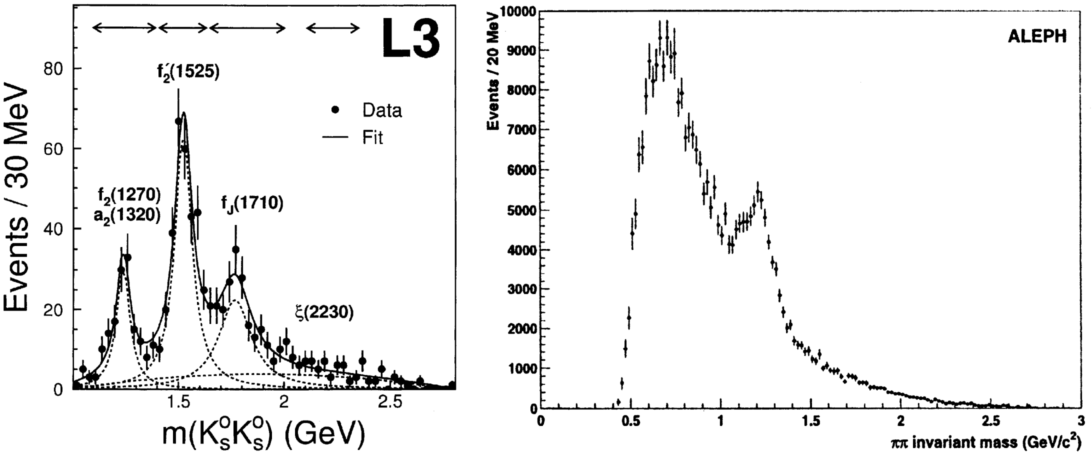

Figure 3.2: Left: K_SK_S mass distribution in $\gamma\gamma$-collisions at LEP/L3 (from ref. [8]); right: $\pi^+\pi^-$ mass distribution from LEP/ALEPH showing only the $f_2(1270)$ (from ref.[9]).

Let us now deal with two-photon processes which are useful to probe the charge content of mesons through their electromagnetic couplings. Glueballs do not couple directly to photons and their production should therefore be suppressed in $\gamma\gamma$-processes. New data in $\gamma\gamma$-collisions have been presented by the LEP collaborations. L3 observes three peaks below 2 GeV in the K_SK_S mass distribution [8] (fig. 3.2, left), but the spin 0 $f_0(1500)$ is not seen. Since $f_0(1500)$ does not couple strongly to $K\bar{K}$, this is perhaps not surprising. However, ALEPH studying the reaction $\gamma\gamma \to \pi^+\pi^-$, does not observe $f_0(1500)$ either [9] (see fig. 3.2, right). An upper limit of 1.4 keV (95 % CL) can be derived for its $\gamma\gamma$-width from the ALEPH result [9], using the known $\pi\pi$ decay branching ratio of the $f_0(1500)$.

The $\gamma\gamma$-width of a $q\overline{q}$ state can be predicted from SU(3). Apart from an unknown nonet constant C and for a meson of mass m:

$$\Gamma_{\gamma\gamma} = C(5\cos\alpha - \sqrt{2}\sin\alpha)^2 m^3\ . \tag{3.2}$$

The $\gamma\gamma$-width of a scalar meson is related to that of the corresponding tensor by

$$\Gamma_{\gamma\gamma}(0^{++}) = k\left(\frac{m_0}{m_2}\right)^3 \Gamma_{\gamma\gamma}(2^{++})\ , \tag{3.3}$$

with obvious notations. Here the factor $k = 15/4$ arises from spin multiplicities in a non-relativistic calculation, while relativistically $k \simeq 2$. Figure 3.1 (right) shows the prediction for the $\gamma\gamma$ partial width of the $f_0(1500)$ as a function of α, together with the ALEPH upper limit [3]. Assuming a $q\overline{q}$ structure, one concludes that $f_0(1500)$ is dominantly $s\overline{s}$ (50° $\leq \alpha \leq$ 100°), at variance with the hadronic results discussed above.

This contradiction indicates that $f_0(1500)$ is not $q\overline{q}$ and the lack of $\gamma\gamma$-coupling points to a large gluonic content. Obviously, some mixing with nearby $q\overline{q}$ states is possible [2] but more accurate data in $\gamma\gamma$-collisions and theoretical guidance on the strength of $\gamma\gamma$-couplings to glueballs are needed

State	Γ [MeV]	Isospin	Nature
$a_0(980)$	~ 50	1	$K\overline{K}, qq\bar{q}\bar{q}$
$f_0(980)$	~ 50	0	$K\overline{K}, qq\bar{q}\bar{q}$
$f_0(600)$	~ 800	0	meson-meson
$\kappa(800)$?	~ 600	1/2	resonances
$a_0(1450)$	265	1	$u\bar{d}, d\bar{u}, d\bar{d} - u\bar{u}$
$f_0(1370)$	~ 400	0	$d\bar{d} + u\bar{u}$
$f_0(1710)$	125	0	$s\bar{s}$
$K_0^*(1430)$	294	1/2	$u\bar{s}, d\bar{s}, s\bar{u}, s\bar{d}$

Table 3.1: Classification of the low-mass scalar mesons showing the scattering resonances below 1 GeV and the ground state $q\overline{q}$ nonet (1^3P_0).

for a more quantitative statement on mixing. Table 3.1 shows an increasingly popular classification scheme for the low lying scalar nonets [10]. The lower mass nonet is made of four-quark states and/or meson-meson resonances. The ground state (1^3P_0 or 0^{++}) $q\overline{q}$ nonet lies in the 1400 MeV region. The supernumerary $f_0(1500)$ (not shown) is dominantly glue.

References

[1] For a review see C. Amsler, Rev. Mod. Phys. **70** (1998) 1293

[2] C. Amsler and F.E. Close, Phys. Rev. **D 53** (1996) 295
see also F.E. Close and A. Kirk, Eur. Phys. J **C 21** (2001) 531

[3] C. Amsler, Phys. Lett. **B 541** (2002) 22

[4] C. Amsler et al., Phys. Lett. **B 353** (1995) 571; **B 342** (1995) 433

[5] A. Abele et al., Phys. Lett. **B 385** (1996) 425

[6] D. Barberis et al., Phys. Lett. **B 479** (2000) 59

[7] C. Amsler et al., Eur. Phys. J. **C 23** (2002) 29

[8] M. Acciarri et al., Phys. Lett. **B 501** (2001) 173

[9] R. Barate et al., Phys. Lett. **B 472** (2000) 189

[10] C. Amsler and N. Törnqvist, Physics Reports (in preparation)

4 Particle Physics with CMS

C. Amsler, A. Dorokhov, C. Hörmann, K. Prokofiev, H. Pruys, C. Regenfus,
P. Robmann, T. Speer, and S. Steiner

In collaboration with: ETH-Zürich, Paul Scherrer Institut (PSI), Universität Basel
and the CMS Collaboration.

4.1 Introduction

We participate in the CMS experiment at the Large Hadron Collider (LHC) where we concentrate on physics involving the b-quark, e.g. b-quark production associated with the formation of Higgs bosons, t-quark decays, and spectroscopy of B mesons. The most interesting events at LHC will contain one or several b-jets originating from the decay of B mesons, with typical mean free paths of a few mm. To allow for efficient tagging of B mesons among the large background of light quark and gluon jets, the detection system has to follow particles towards the primary vertex. The silicon pixel detector we are developing is the closest detector to the interaction point, located only 4 cm from the beam-beam interaction point. The extremely high particle flux near the primary vertex ($\sim$ 1000 particles every 25 ns) requires the innermost tracking layers to be composed of pixel devices delivering 3D coordinates with high resolution and no ambiguity. Furthermore, the radiation dose to the nearest detector will approach 10^6 Gy (corresponding to 6×10^{14} hadrons /cm^2) after 10 years of LHC operation. This is about 10^6 more than for detectors developed earlier for space research.

Our group contributes to the design, construction and test of the pixel sensors, the readout chips and the mechanical support structure, and we are also involved in the event reconstruction software.

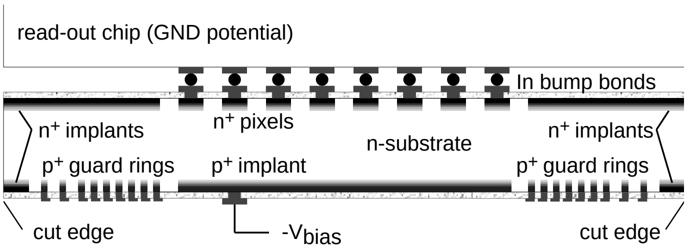

Figure 4.1: *Design of a sensor connected to the readout chip. The bias voltage is applied to the backside.*

4.2 Pixel sensors

The barrel pixel detector consists in three concentric cylindrical layers, 53 cm long with radii of 4.4, 7.3 and 10.2 cm. The layers contain some 3×10^7 silicon pixels. Coverage in the beam direction is achieved with forward/backward wheels provided by the U.S. participants. The pixel modules consist of thin, segmented sensor plates with highly integrated readout chips connected by the indium bump bonding technique. Figure 4.1 shows a sketch of the sensor/chip assembly. The pixel size was recently reduced from 150 $\times$ 150 μm^2 to 125 $\times$ 125 μm^2 and rectangular pixels of 150 $\times$ 100 μm^2 are being considered for the final design. The analogue signals are read out to determine the coordinates more accurately, using charge sharing between adjacent pixels.

For n^+ implants in n-material the pixels have to be isolated from one another. This is usually done with one or several narrow p^+-rings around each pixel (the so-called p-stop rings). To avoid excessive charging of an unbonded pixel (one with poor indium connection to the chip) leading to local discharges and momentary failures of whole pixel clusters, the resistance between pixels should remain finite. A narrow resistive path between the pixels would prevent the pixels from charging up. This is accomplished by small openings in the p-rings which lead to atoll-like structures made of one or several rings surrounding each pixel (see fig. 4.5) below. More details can be found in previous annual reports, in the technical design report [1] and in a recent PhD thesis [2].

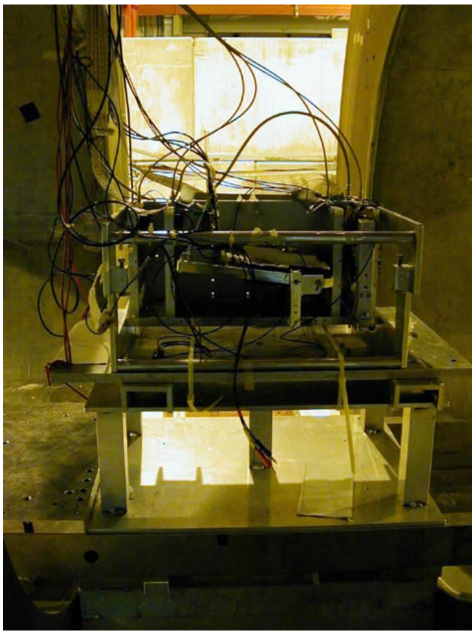

Figure 4.2: *Setup for the sensors test. The pixel detectors are located at the center of the silicon telescope. The two supraconductive coils are visible at the edges of the picture.*

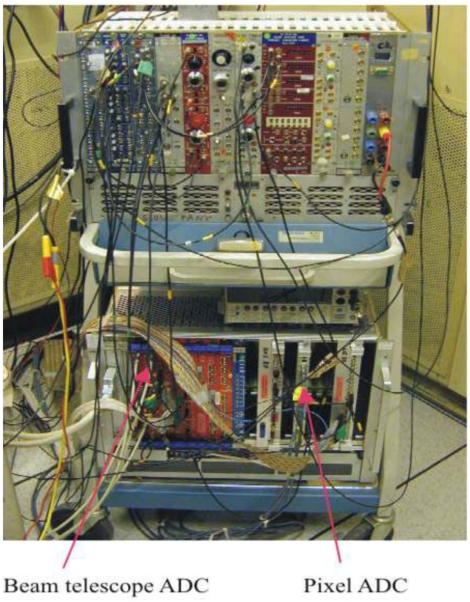

Figure 4.3: *Readout and control system.*

In 2002 we ordered with CiS Erfurt a batch of sensors with various atoll designs, some oxygenated (oxygen is known to reduce the acceptor concentration after type inversion and hence also the required depletion voltage). In some of the sensors the p-stop rings were missing. Instead, the p implant was not spatially defined by a mask, but sprayed over the whole wafer with moderate concentration.

A first test of this batch was performed by the Zurich group in July 2002 using 225 GeV pions from the CERN-SPS. The purpose of the test was to measure (i) the position resolution, (ii) the charge collection efficiency, and (iii) the Lorentz deflection angle in the 4 T field foreseen at CMS. The pixel detector was located at the center of our microstrip telescope [3], so that pions would traverse the detector at a grazing angle $\alpha = 15^\circ$ (fig. 4.2). Our telescope is made of 8 layers of x and y silicon microstrips (50 μm pitch size). Through charge division between neighbouring strips the telescope is capable of measuring the space coordinates of an incident charged particle with an r.m.s. resolution of 1 μm [3]. A fast trigger diode (less than $20 ns$ rise time) provided the trigger. The silicon sensor was bump bonded to the readout chip (PSI30, DMILL/Honeywell) and was read out through VME ADC's by a LabView program. The data acquisition system is shown in fig. 4.3.

The apparatus was immersed in a longitudinal magnetic field provided by two Helmholtz coils to measure the Lorentz angle Θ_L: due to deflection in the magnetic field the charge carriers do not move along the electric field lines but drift at an angle Θ_L towards adjacent pixels. The charge deposit is therefore shared among (mostly two) adjacent pixels. The Lorentz angle can be measured by finding the coordinate z of the pixel row for which the charge collected between the main and adjacent pixels are equal (fig. 4.4 right). This corresponds to charge reaching the readout surface between two pixels. The coordinate Δy of the impinging track is determined by the telescope and Θ_L can be

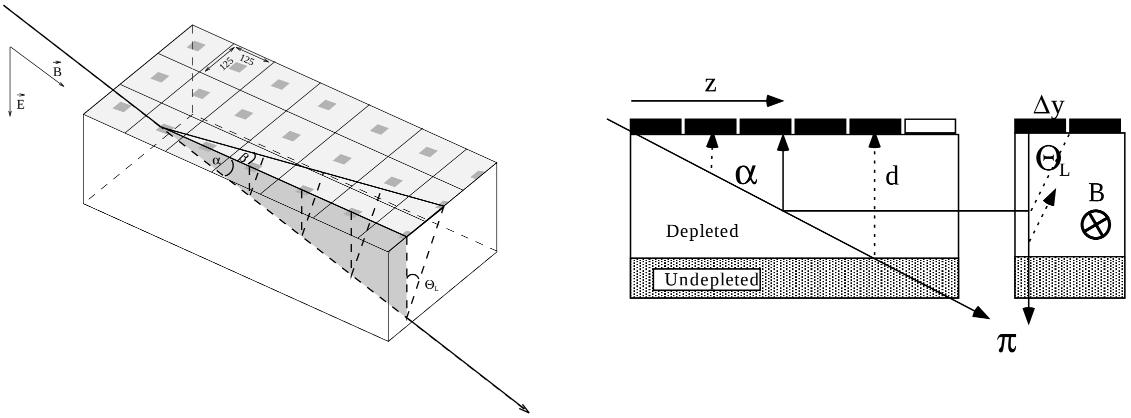

Figure 4.4: *Left: three dimensional sketch of the pixel detector traversed by a charged particle under the grazing angle α. The Lorentz angle is denoted by Θ_L. Right: determination of the Lorentz angle Θ_L (see text).*

calculated from the relation tanΘ_L = Δy/z tanα. Note that for irradiated pixels after type inversion the depletion layer grows from the readout side (as shown in fig. 4.4, right). The depletion thickness can be determined from the length of the hit pixels along the incident direction. Similar studies were performed earlier by our group [2, 4]. However, several design parameters for the sensors have changed since then: we have now somewhat smaller pixel sizes, atoll-like p-stop rings and a different supplier. Also the pixels are now bump-bonded to a semifinal version of the readout chip.

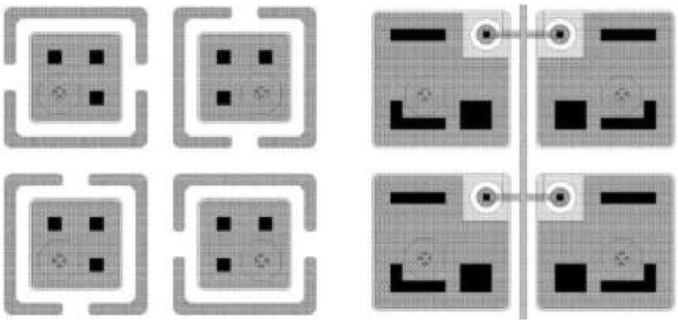

Figure 4.5: *The two pixel layouts tested in 2002: p-stop (left) and p-spray (right).*

Data were collected with two detectors made of 32 × 22 bump bonded pixels (125 × 125 μm^2), one with p-stop rings and one with p-sprays (fig. 4.5). Irradiated pixels could not be tested reliably because we could not reach the operating temperature of -10° foreseen at CMS. During two weeks of beam time we collected some 6 × 10^6 events. The analog amplitudes from the pixels had first to be corrected for common mode noise. The hit coordinates for the strips and pixels were obtained from the average hits weighted by the hit amplitudes. After the alignment, the hit position of the incident particle on the pixel sensors was known with a (moderate) precision of $\approx 5\mu$m. Figure 4.6 shows the correlation between hit coordinates in the microstrips and pixel detectors.

The charge collected by one pixel depends on the incident track. On the borders of the pixel the charge is shared between few (mostly two) pixels, hence the collected charge in the tested pixel is smaller. The average charge collected by one pixel as a function of track position can be used to calculate the lateral charge diffusion in the silicon bulk. The charge distribution is a convolution of the charge diffusion function with the size of the pixel. The average charge collected by one pixel as a function of the track position in the x and y directions on the pixel surface is shown in fig. 4.7 (left). The detector was oriented with its surface perpendicular to the incident beam and the magnetic field was off. The deconvoluted lateral charge distribution during the charge drift through the 280

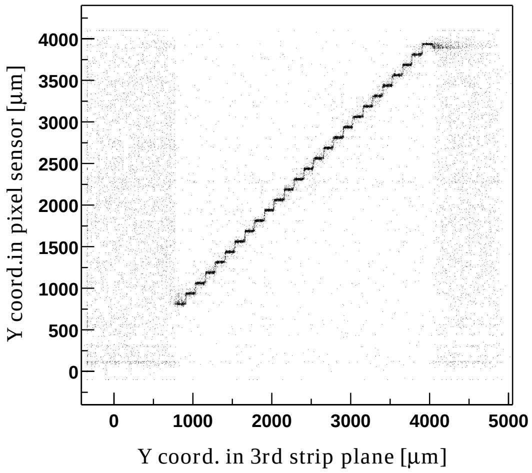

Figure 4.6: *Vertical hit coordinate in the third strip detector vs. vertical hit coordinate in the pixel sensors. The steps are due to the much smaller pitch of the microstrip detector. The dark bands left and right are due to open readout channels.*

μm thick silicon is shown in fig. 4.7 (right), together with a gaussian fit. The lateral diffusion has an r.m.s. width of about 15 μm.

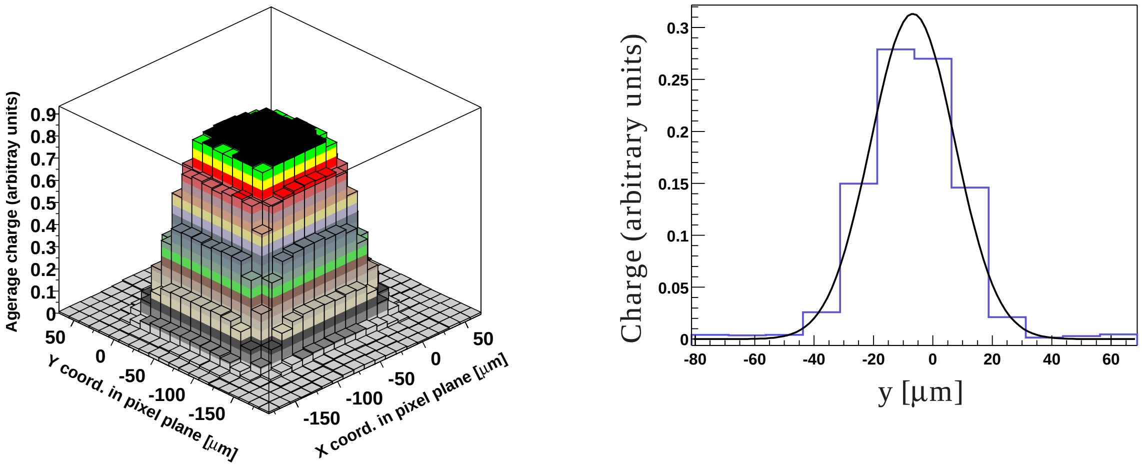

Figure 4.7: *Left: average collected charge by one pixel in the absence of magnetic field. Right: lateral charge distribution due to diffusion in the 280 μm thick silicon, together with gaussian fit.*

Figure 4.8 (left) shows the distribution of charge with magnetic field. The pixel detector was oriented with its surface at a grazing angle of 15° and the field was 3 T. One can see that the charge migrates slightly to the left of the incident track. The coordinate of average energy deposit is shown in fig. 4.8 (right) as a function of track length y. The Lorentz angle calculated for the non-irradiated sensor is about 16° at 3 T and 21° at 4 T.

Finally, we measured the position resolution of the pixel detector. In the CMS detector the tracks hitting the pixel barrel are on average perpendicular to the magnetic field. However, the field was parallel to the beam during our test. To simulate charge sharing due to the magnetic field, the detector surface was therefore tilted by an angle of 65° with respect to the beam direction to simulate the Lorentz deflection. In the vertical direction the charge was shared by several pixels while in the horizontal direction the charge was collected by single pixels (except for tracks in the border regions for which charge was collected by two adjacent pixels). The measured coordinate was obtained by weighting the pixel hits with their amplitudes. Figure 4.9 shows the residuals between measured and predicted hits from the telescope in the horizontal (left) and vertical (right) directions. In the

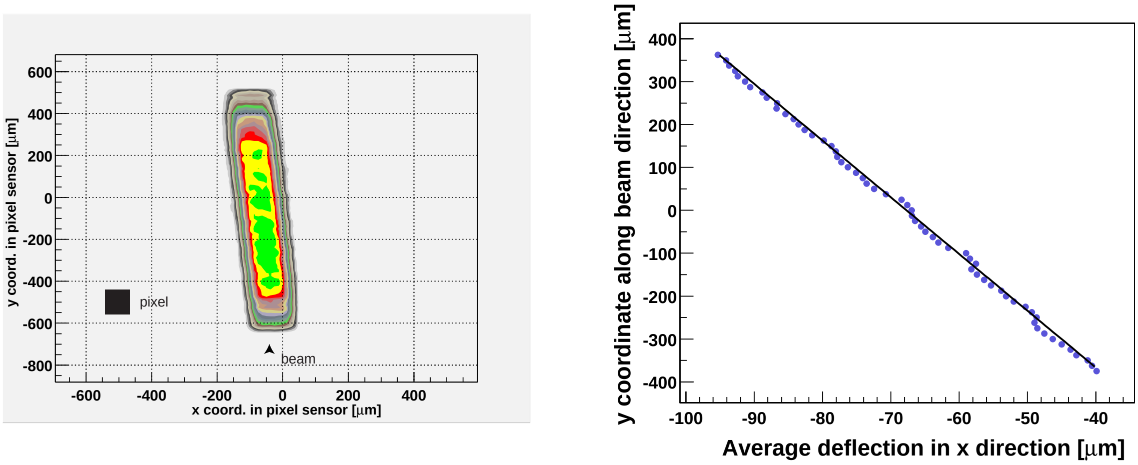

Figure 4.8: *Left: distribution of collected charge on the surface of the silicon sensor for grazing tracks. The y coordinate is along the beam direction. Right: average deflection as a function of detected track length along the beam direction.*

horizontal direction the resolution is about $\sigma \simeq 34$ μm, as expected from a box distribution for 125 μm broad pixels. In the vertical direction, however, the resolution is much better thanks to charge sharing: $\sigma \simeq 11$ μm.

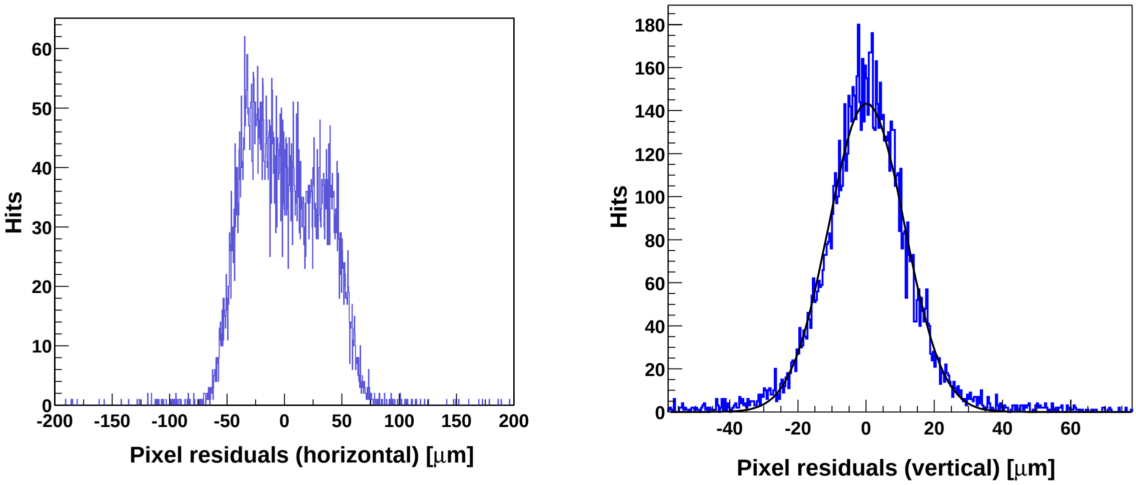

Figure 4.9: *Residuals in horizontal (left) and in vertical (right) direction between measured and predicted coordinates, showing the enhanced resolution obtained with charge division.*

Another important aspect is the signal-to-noise ratio. The energy deposit for minimum ionizing particles was measured for perpendicular incidence. The resulting Landau distribution was compared to the (gaussian) noise distribution. We obtained a signal-to-noise ratio of 130.

4.3 Readout chip

During summer 2002 we also tested in a high intensity pion beam of 350 MeV/c at PSI the CMS Read Out Chip (ROC) which was designed in radiation hard DMILL technology. For that test we used the PSI43 chip, the first ROC that contained the complete functionality and the foreseen number of pixels (52 columns $\times$ 53 rows of pixels). We were able to test the chip-sensor unit under rates comparable to those expected at LHC.

In 2002 we also received our first test structures, which were processed in quarter micron technology (Deep Sub Micron, DSM). A complete redesign of the existing chip was necessary but this technology has the following advantages: DSM chips are cheaper since the process is well known and used widely by the conventional chip industry. DSM technology also offers new possibilities in designing the chip and improving its performances. There are for example five metal layers available for routing instead of only two and the smallest structure is only 0.25 μm wide, compared to 0.8 μm in DMILL. Thus we will be able to increase the number of data buffers from 24 to 32 and thereby reduce data loss. Another benefit is the low power consumption as DSM needs only half the supply voltage and half the current of DMILL. Thus, as will be shown below, the power consumption is four times lower for the same speed. We also expect a higher yield than in case of DMILL and the radiation hardness is excellent.

We have performed measurements with test structures of the analog block that were designed in DSM technology. Figure 4.10 (left) shows the schematics of the analog block test structure.

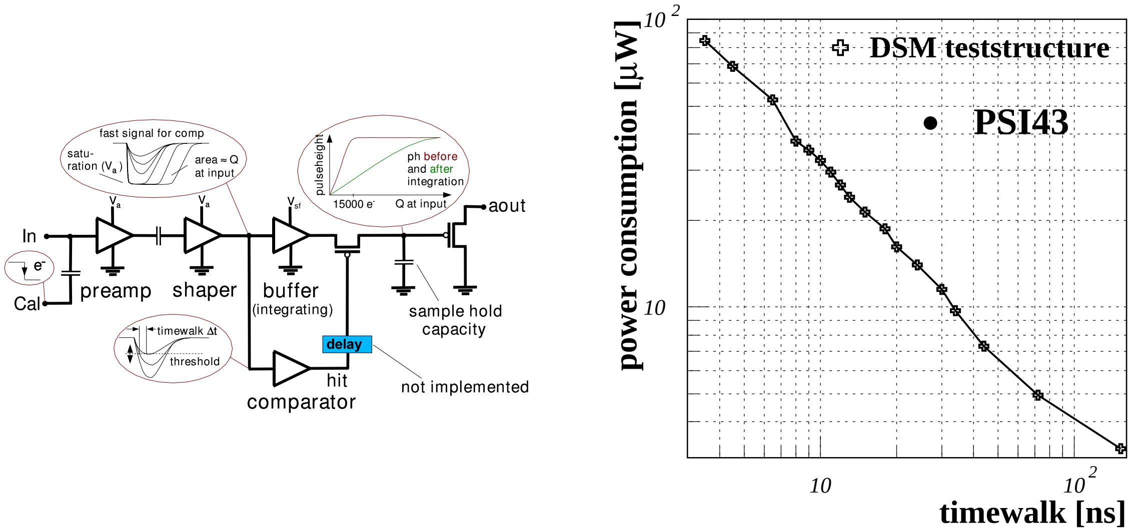

Figure 4.10: *Left: layout of the analog block test structure. Right: power consumption versus timewalk.*

It consists of two stages, a charge sensitive preamplifier and a shaper. Both stages have to be very fast because of the 40 MHz bunch crossing frequency at LHC. An extra amplifier integrates the signal to deal with saturated shaper output signals. These amplifier stages are followed by the sample and hold capacity and an output driver. A comparator, integrated in the analog block, generates the hit signal when the output level of the shaper is higher than the input threshold of the comparator. The hit signal is needed for storing the pulse height in the sample and hold capacity until the readout sequence is completed.

A very important measurement was power consumption versus timewalk (fig. 4.10, right). A low power consumption is important, because each μW/pixel leads to about 60 Watt for the entire pixel detector. As fig. 4.10 shows, power consumption decreases rapidly with timewalk. However, when the latter exceeds 25 ns the event is assigned to the wrong bunch crossing. For test structure A we obtained a power consumption of 14 μW for a timewalk of 25 ns. This is much smaller than for the DMILL design (40μW) advocated in the design report [1].

Figure 4.11 shows the output signal of the shaper and the analog output signal aout (see the layout in fig. 4.10) caused by a charge injected at the calibration input. The tests tructures were irradiated with a ^{60}Co γ-source (132 kGy) at PSI. The red curves were measured before irradiation, the black ones after radiation and the green ones after readjusting the settings for the preamp and shaper. Hence

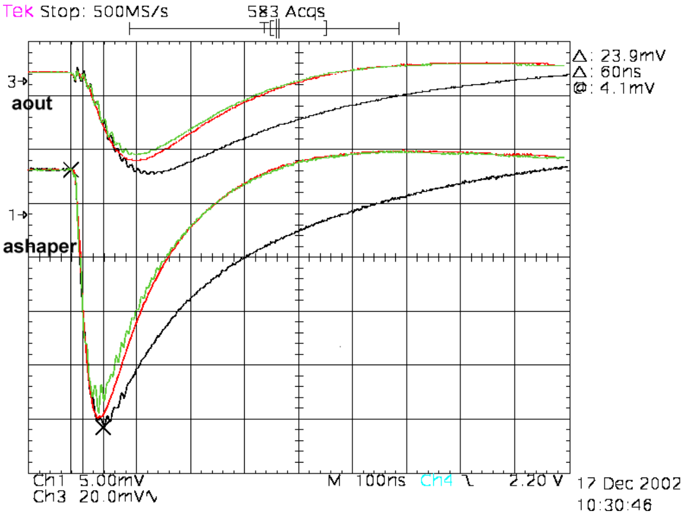

Figure 4.11: *Analog out of the shaper and aout (see also fig. 4.10) before (red) and after (black) irradiation, and after compensation (green).*

we were able to compensate for the irradiation damages, leading to an increase in gain and decay time, by readjusting the settings.

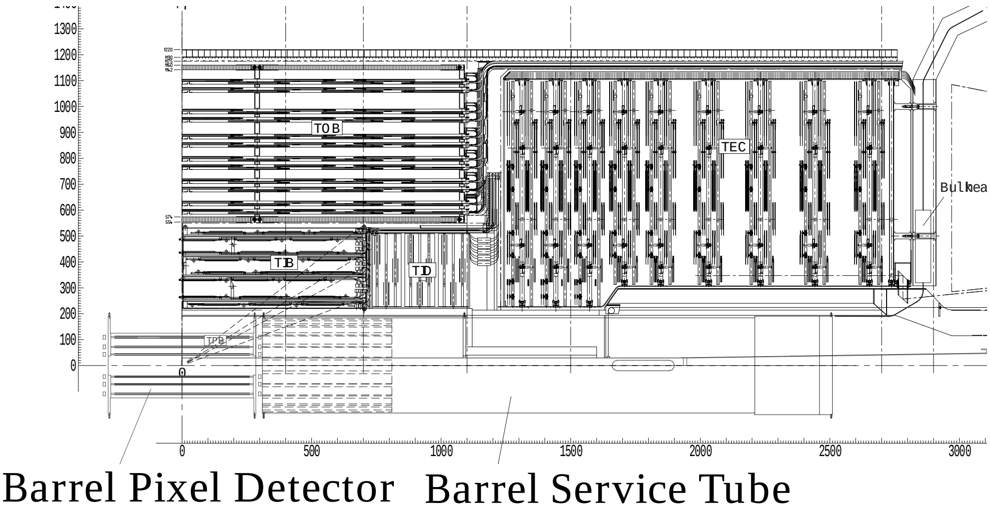

Figure 4.12: *A quarter of the CMS tracking system with the barrel pixel detector in the center and the service tube in z-direction.*

4.4 Mechanical support structure

Our group and our institute's workshop (see also the report from the mechanical workshop) are involved in the design and construction of the mechanical support structure for the detector and the service tube in beam direction. Figure 4.12 shows a sketch of a quarter of the CMS tracking system. The three layers of the pixel detector are shown, together with the 220 cm long service tube. The system has a total length of 5 m. Since the LHC beampipe will already be present during installation of the pixel detector, two vertically separated pixel half shells will be introduced on a dedicated rail system (see also fig. 4.17 below).

The detector support structure (fig. 4.13) will be made of pure aluminum tubes with trapezoidal shapes to fit the geometrical constraints and a wall thickness of only 0.3 mm. Custom made, 0.24 mm thick, carbon fiber blades, which support the pixel modules, will then be glued to the tubes forming

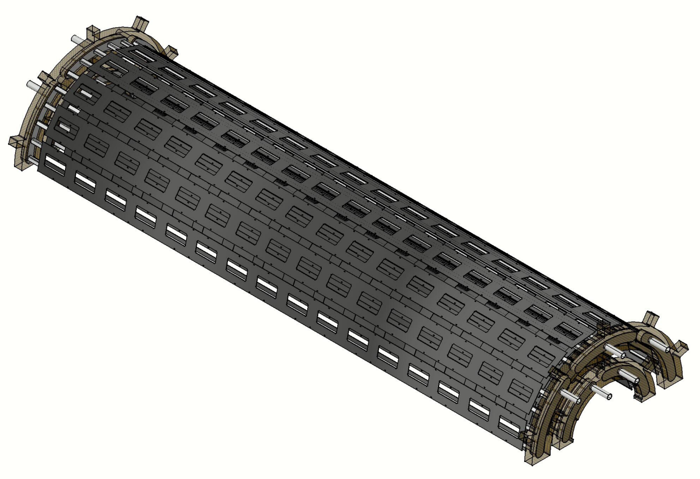

Figure 4.13: *View of the support structure for the inner and middle layers of pixel sensors. The extremities of the half shells with the embedded cooling manifolds are also shown.*

the detector segments. Four to five of this tubes will be connected with a laser welding technique to an aluminum container which distributes the cooling fluid. Figure 4.14 shows a picture of such a welding seem taken with a microscope. Note that the width of the seem is only about $3/10$ of a millimeter. The resulting manifold will provide the necessary cooling of the detector modules to -10^{0}C with C_6F_{14}. At both ends the manifolds are embedded in a carbon fibre support frame as illustrated in fig. 4.13.

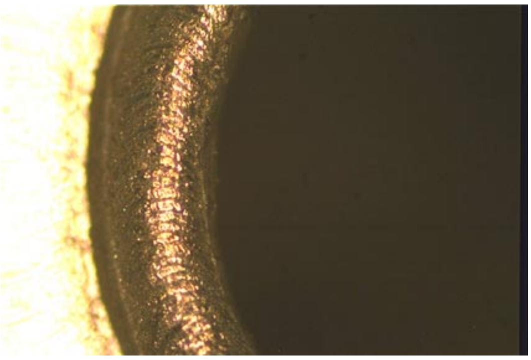

Figure 4.14: *High quality welding seem between a cooling tube (right side) and the container (left side).*

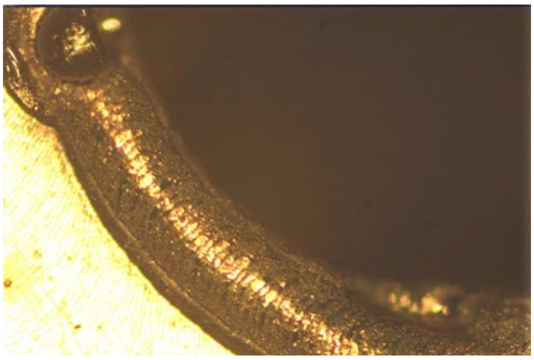

Figure 4.15: *Bad welding seem with a hole and a gap.*

The laser welding is done in close collaboration with an external company. Tests gave promising results (fig. 4.14). However, we realized that the tool used was not precise nor massive enough. Figure 4.15 shows a problematic zone with holes and gaps. This happens when the laser beam misses the working piece or when there is an excessive gap between the parts that have to be welded. The tests indicated also that the physical and chemical properties of the different pieces have to be of the same quality.

A complete detector segment was manufactured with an improved welding tool consisting of massive copper pieces supporting the segment structure during the welding process. The new tools guarantee the required precision and remove the heat during the welding process. The segment of the barrel pixel support structure was installed in a container and flushed with dry nitrogen for cooling tests (fig. 4.16). Mechanical survey and cooling tests will have to be performed to prove that the technique meets all requirements.

The two service tubes in $+z$ and $-z$ direction, which enclose the end cap pixel detector system

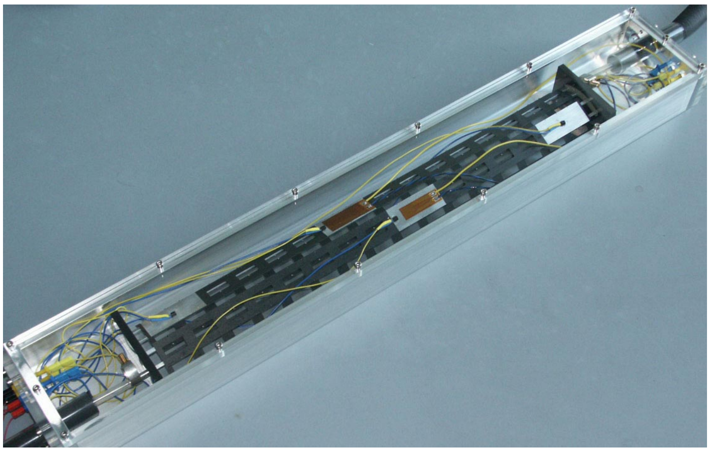

Figure 4.16: *Detector segment in its dry nitrogen container. Note the resistors to simulate the power loss and the temperature sensors mounted on the carbon fibre blades.*

(fig. 4.17), connect the barrel pixel detector to the tracking system. They transfer the power, the optical and electrical signals and the cooling fluid to the detector. To minimize multiple scattering we will use aluminum wires, which are plated with a thin copper layer for the power lines and aluminum for the cooling tubes. The motherboards which hold the optical hybrids for the analog and control links are integrated at the detector end. The power regulators are mounted at the outer ends. A honeycomb support structure is foreseen (fig. 4.18) to minimize the amount of material and to guarantee sufficient stability.

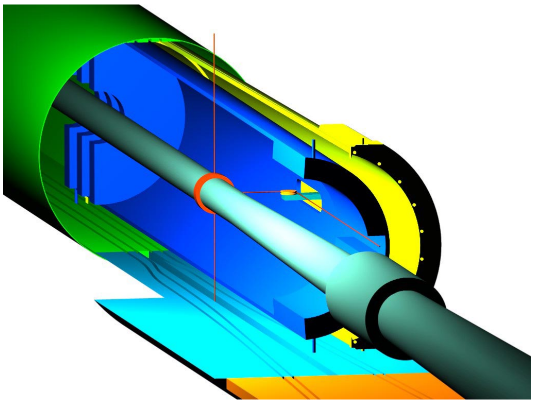

Figure 4.17: *View of the CMS beampipe surrounded by the pixel detector service tubes for the barrel detector (yellow) and the end cap discs (blue).*

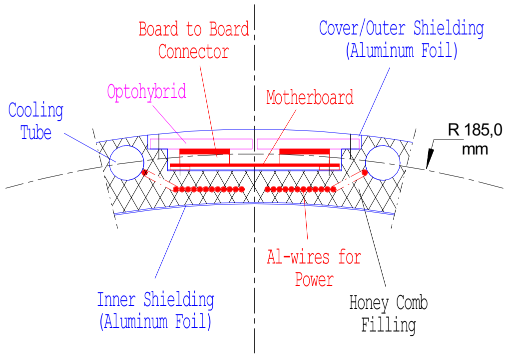

Figure 4.18: *Cross section of the service tube near the pixel detector flange, showing the motherboards which hold the optical hybrids.*

4.5 CMS event reconstruction

We are participating in the track reconstruction software and, in particular, in the vertex reconstruction techniques in the object-oriented reconstruction framework ORCA. We have implemented a single-vertex fit algorithm using the Kalman filter formalism. This algorithm is often used both in track [6] and vertex reconstruction [7].

So far, only a simplified version [5, 8] of a Kalman filter had been implemented. Tracks were assumed to be straight in the vertex neighbourhood. This considerably simplified the algorithm and reduced the computation time but did not allow the tracks to be refitted as emerging from a common vertex. In our improved version of the filter realistic helicoidal track models are used. Track parameters may then be recalculated with the additional vertex constraint, providing a full track-to-track covariance matrix.

The r.m.s.resolution of the reconstructed vertex in the Higgs decay $H^0 \rightarrow Z^0 Z^0 \rightarrow \mu^+\mu^-\mu^+\mu^-$ is approximately 12 μm in the transverse direction and 19 μm in the longitudinal (z) direction. For decays of B_s mesons the corresponding resolutions are 55 μm and 73 μm, respectively (fig. 4.19). While no improvement is gained on the resolution itself, the full Kalman filter algorithm is up to four times faster than the linearized version. This is interesting in view of its possible application to the online high-level trigger.

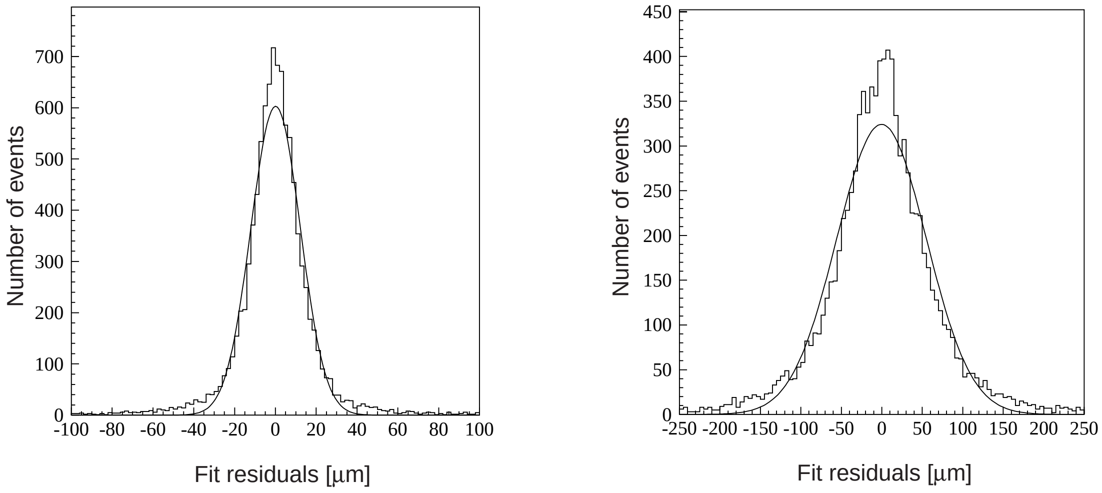

Figure 4.19: *Expected resolution in the transverse direction for the reconstructed decay vertex in* $H^0 \rightarrow Z^0 Z^0 \rightarrow \mu^+\mu^-\mu^+\mu^-$ *(left) and in* $B_s \rightarrow J/\psi\phi$ *(right).*

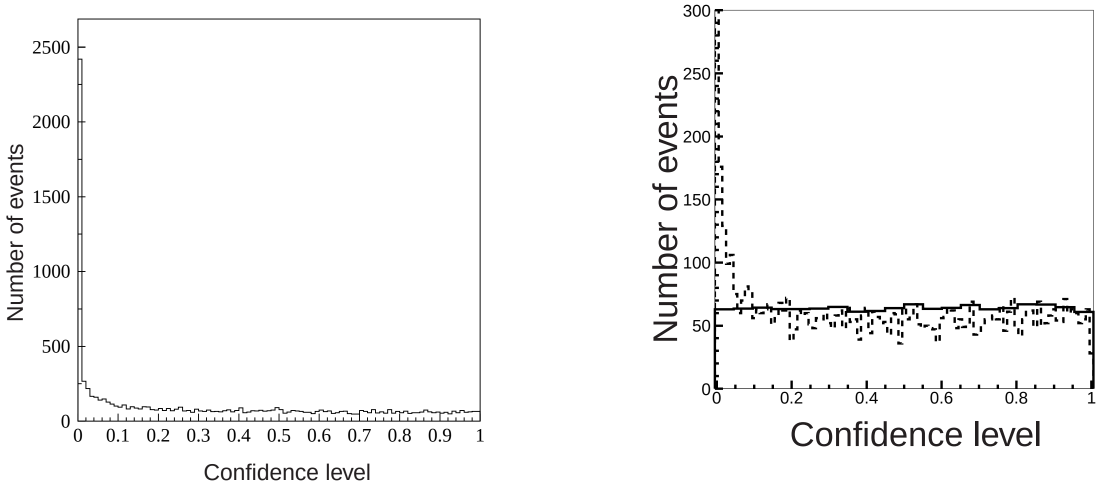

Figure 4.20: *Left: expected confidence level distribution for the decay* $H^0 \rightarrow Z^0 Z^0 \rightarrow \mu^+\mu^-\mu^+\mu^-$. *Right: confidence level distribution for tracks with perfectly gaussian track parameters (full line) and tracks affected by 3% non-gaussian tails (dashed line).*

Nevertheless, the distributions of the confidence level (fig. 4.20, left) show a large peak at low confidence level. This is due to the track parameters which have non-gaussian tails, as demonstrated in fig. 4.20 (right). To alleviate this problem, we are developing a gaussian sum filter (GSF) for vertex fitting, in which the distributions of the track parameters are modelled by superpositions of gaussians describing the core and the tails. The GSF is then a weighted sum of several Kalman filters, and it can be implemented as a number of Kalman filters run in parallel.

We have also started to develop a kinematic fit in which additional constraints (such as masses of decaying particles, momentum and energy conservation) are incorporated into the vertex fit. We are able to reconstruct intermediate particles coming from sequential decays by imposing kinematic constraints on the final state particles. For example one can reconstruct complete decay chains, such as the decays $B^- \rightarrow D^0 l^- \bar{\nu}_l$, followed by $D^0 \rightarrow K^- \pi^+$, $D^0 \rightarrow K^- \pi^+ \pi^0$ or $D^0 \rightarrow K^- \pi^+ \pi^- \pi^+$, where only the final longlived particles are reconstruced in the detector. This procedure can also improve the experimental resolutions.

References

[1] CMS - The Tracker Project, Technical Design Report, CERN LHCC 98-6, CMS TDR 5 (1998)
[2] R. Kaufmann, PhD Thesis, Universität Zürich, 2001
[3] C. Amsler *et al.*, Nucl. Instr. Methods in Physics Res. **A 480** (2002) 501
[4] B. Henrich and R. Kaufmann, Nucl. Instr. and Methods in Phys. Res. **A 304** (2002) 304
[5] P. Billoir and S. Qian, Nucl. Instr. Methods in Phys. Res. **A 311** (1992) 139
[6] R. Frühwirth, Nucl. Instrum. and Methods in Phys. Res. **A 262** (1987) 444
[7] R. Frühwirth, R. Kubinec, W. Mitaroff and M. Regler, Comp. Phys. Comm. **96** (1996) 189
[8] V. Karimäki, “Effective Vertex Fitting”, CMS note 1997/051.

5 Publications

Articles

- A new measurement of the $\bar{\nu}_e e^-$ elastic cross section at very low energy
  C. Amsler et al. (MUNU collaboration)
  Phys. Lett. B 545 (2002) 57

- Sub MeV particles detection and identification in the MUNU detector
  M. Avenier et al. (MUNU collaboration)
  Nucl. Instr. and Methods in Phys. Research A 482 (2002) 408

- Production and detection of cold antihydrogen atoms
  M. Amoretti et al. (ATHENA collaboration)
  Nature 419 (2002) 456

- Non-$q\bar{q}$ mesons
  C. Amsler
  Phys. Rev. D 66 (2002) 010001-754

- The η(1440), f_1(1420), and f_1(1510)
  M. Aguilar-Benitez, C. Amsler and A. Masoni
  Phys. Rev. D 66 (2002) 010001-493

- Comment on “Protonium annihilation into $\pi^0\pi^0$ at rest in a liquid hydrogen target”
  C. Amsler et al. (Crystal Barrel collaboration)
  Phys. Rev. D 66 (2002) 058101

- Further evidence for a large glue component in the $f_0(1500)$ meson
  C. Amsler
  Phys. Lett. B 541 (2002) 22

- Review of Particle Physics
  K. Hagiwara et al. (Particle Data Group)
  Phys. Rev. D 66 (2002) 010001

- Particle data booklet
  K. Hagiwara et al. (Particle Data Group)
  AIP pub. 72 (2002)

- Upgrade of the ATHENA Detector with Avalanche Photodiodes and Quantum Efficiency Measurements at Cryogenic Temperatures
  A. Glauser
  Diplomarbeit, Universität Zürich, 2003

- A high resolution silicon beam telescope
  C. Amsler et al.
  Nucl. Instr. Methods in Physics Research A 480 (2002) 501

- Temperature dependence of pure CsI: scintillation light yield and decay time
  C. Amsler et al.
  Nucl. Instr. Methods in Physics Research A 480 (2002) 494

- Meson Resonances in Proton-Antiproton Annihilation
  C. Amsler
  Proc. Int. Conf. on the Structure and Interactions of the Photon (PHOTON 2001), Ascona, World Scientific (2001) 253

- The Atlas and CMS trackers
  T. Speer
  Proc. 5th Int. Conf. on Hyperons, Charm and Beauty Hadrons, Vancouver (2002)
  Nucl. Phys. B (Proc. Suppl.) 115 (2003) 318

- Tracking in CMS : software framework and tracker performance
  A.I. Khanov, M. Lenzi, T. Todorov, T. Speer, P. Vanlaer and M. Winkler
  Nucl. Instr. and Methods in Phys. Research A 478 (2002) 460

Articles in press

- Annihilation at rest of antiprotons and protons into neutral particles
  C. Amsler et al. (Crystal Barrel Collaboration)
  Phys. Lett. B

- Positron plasma diagnostics and temperature control for antihydrogen production
  M. Amoretti et al. (ATHENA collaboration)
  Phys. Rev. Lett.

- Light exotic mesons
  C. Amsler
  Proc. Quark Confinement and the Hadron Spectrum V, Gargnano, 2002
  World Scientific

- A cryogenic silicon microstrip and pure-CsI detector for detection of antihydrogen annihilations
  C. Regenfus
  Proc. Int. Workshop (Vertex 2001), Brunnen
  Nucl. Instr. and Methods in Phys. Research A

- C. Regenfus, C .Amsler, A. Glauser, D. Grögler, D. Lindelf, H. Pruys
  Detection of antihydrogen annihilations with a cryogenic pure-CsI detector
  Proc. of “New developments in photodetection”, Beaune 2002
  Nucl. Instr. and Methods in Phys. Research A

- A. Glauser
  Development of APD readout for pure-CsI crystals at cryogenic temperatures
  Proc. of “New developments in photodetection”, Beaune 2002
  Nucl. Instr. and Methods in Phys. Research A

- New Developments in Vertex Reconstruction for CMS
  R. Frühwirth, K. Prokofiev, T. Speer, P. Vanlaer and W. Waltenberger
  Nucl. Instr. and Methods in Phys. Research A

Invited Lectures

- C. Amsler
  Seminar, Università di Genova,, 19.4.02
  “New results in proton-antiproton annihilation and the status of glueballs”

- C. Amsler
  Università degli Studi di Pavia, 17.4, 18.4 and 23.4.02
  "The spectrum of light quark-antiquark mesons"

- C. Amsler
  Seminar, Helsinki University, 27.8.02
  "New results in proton-antiproton annihilation and the status of glueballs"

- C. Amsler
  Invited talk, Quark Confinement and the Hadron Spectrum V, Gargnano, 12.9.02
  "Light exotic mesons"

- C. Amsler
  Invited talk, Aspects of confinement and nonperturbative QCD, ECT* Center, Trento, 14.3.03
  "Experimental evidence for a large glue content in the $f_0(1500)$ meson"

- C. Amsler
  Seminar, Universität Basel, 16.01.03
  "Glueballs and other exotic mesons"

- O. Link
  Contributed talk, Workshop on large TPC for low energy rare event detection, 5.12.02
  "The MUNU experiment"

- N. Madsen
  Seminar, Center for Ultracold Atoms, MIT, Cambridge, USA, 15.10.02
  "First production of cold antihydrogen"

- C. Regenfus
  Seminar, PSI, 26.4.02
  "Detection of antihydrogen atoms in the ATHENA experiment with a cold Si-μ-strip and pure CsI detector"

- C. Regenfus
  Seminar, Universität Basel, 31.10.02
  "First production and detection of cold antihydrogen"

- C. Regenfus
  Plenary talk, Frühjahrstagung der DPG, Aachen, 13.03.03
  "Production of cold antihydrogen atoms in large quantities"

- T. Speer
  Invited talk, 5th Int. Conf. on Hyperons, Charm and Beauty Hadrons, Vancouver, 28.06.03
  "The ATLAS and CMS Trackers"

ATHENA Collaboration (2002):
M. Amoretti, C. Amsler, G. Bonomi, A. Bouchta, P. Bowe, C. Carraro, C. L. Cesar, M. Charlton, M. J. T. Collier, M. Doser, V. Filippini, K. S. Fine, A. Fontana, M. C. Fujiwara, R. Funakoshi, P. Genova, J. S. Hangst, R. S. Hayano, M. H. Holzscheiter, L. V. Joergensen, V. Lagomarsino, R. Landua, D. Lindelöf, E. Lodi Rizzini, M. Macri, N. Madsen, G. Manuzio, M. Marchesotti, P. Montagna, H. Pruys, C. Regenfus, P. Riedler, J. Rochet, A. Rotondi, G. Rouleau, G. Testera, A. Variola, T. L. Watson, D. P. van der Werf

MUNU Collaboration (2002):
C. Amsler, M. Avenier, C. Broggini, J. Busto, C. Cernac, Z. Daraktchieva, G. Gervasio, P. Jeanneret, G. Jonkmans, D.H. Koang, J. Lamblin, D. Lebrun, O. Link, F. Ould-Saada, G. Puglierin, A. Stutz, A. Tadsen, J.L. Vuilleumier

CRYSTAL BARREL Collaboration (2002):
C. Amsler, C. A. Baker, B. M. Barnett, C. J. Batty, M. Benayoun, P. Blüm, K. Braune, D. V. Bugg, T. Case, V. Credé, K. M. Crowe, M. Doser, W. Dünnweber, D. Engelhardt,M. A. Faessler, R. P. Haddock, F. H. Heinsius, M. Heinzelmann, N. P. Hessey, P. Hidas, D. Jamnik, H. Kalinowsky, P. Kammel, J. Kisiel, E. Klempt, H. Koch, M. Kunze, U. Kurilla, R. Landua, H. Matthäy, C. A. Meyer, F. Meyer-Wildhagen, R. Ouared, K. Peters, B. Pick, M. Ratajczak, C. Regenfus, J. Reinnarth, W. Roethel, A. Sarantsev, S. Spanier, U. Strohbusch, M. Suffert, J. S. Suh, U. Thoma, I. Uman, S. Wallis-Plachner, D. Walther, U. Wiedner, K. Wittmack, and B. S. Zou

PARTICLE DATA Group (2002):
K. Hagiwara, K. Hikasa, K. Nakamura, M. Tanabashi, M. Aguilar-Benitez, C. Amsler, R.M. Barnett, P.R. Burchat, C.D. Carone, C. Caso, G. Conforto, O. Dahl, M. Doser, S. Eidelman, J.L. Feng, L. Gibbons, M. Goodman, C. Grab, D.E. Groom, A. Gurtu, K.G. Hayes, J.J. Hernandez-Rey, K. Honscheid, C. Kolda, M.L. Mangano, D.M. Manley, A.V. Manohar, J. March-Russell, A. Masoni, R. Miquel, K. Mönig, H. Murayama, S. Navas, K.A. Olive, L. Pape, C. Patrignani, A. Piepke, M. Roos, J. Terning, N.A. Törnqvist, T.G. Trippe, P. Vogel, C.G. Wohl, R.L. Workman, W.-M. Yao